THERMAL AND MECHANICAL PHENOMENA IN ALIGNED CARBON

NANOTUBE FILMS

A DISSERTATION

SUBMITTED TO THE DEPARTMENT OF MECHANICAL ENGINEERING

AND THE COMMITTEE ON GRADUATE STUDIES

OF STANFORD UNIVERSITY

IN PARTIAL FULFILLMENT OF THE REQUIREMENTS FOR THE DEGREE OF

DOCTOR OF PHILOSOPHY

Yuan Gao

August 2012

This dissertation is online at: http://purl.stanford.edu/tk547vj0224

I certify that I have read this dissertation and that, in my opinion, it is fully adequate in scope and quality as a dissertation for the degree of Doctor of Philosophy.

Kenneth Goodson, Primary Adviser

I certify that I have read this dissertation and that, in my opinion, it is fully adequate in scope and quality as a dissertation for the degree of Doctor of Philosophy.

Wei Cai

I certify that I have read this dissertation and that, in my opinion, it is fully adequate in scope and quality as a dissertation for the degree of Doctor of Philosophy.

Thomas Kenny

Approved for the Stanford University Committee on Graduate Studies.

Patricia J. Gumport, Vice Provost Graduate Education

This signature page was generated electronically upon submission of this dissertation in electronic format. An original signed hard copy of the signature page is on file in University Archives.

Abstract

Efficient heat conduction is critical to the performance and reliability of a variety of devices. To ensure efficient heat removal from electronic devices, thermal interface materials (TIMs) are used to enhance heat conduction between two contacting surfaces. Ideal TIMs have high thermal conductivity, conform to the microscale roughness of the surfaces in contact, and accommodate stresses due to mismatch in thermal expansion coefficients. Commercial TIMs exhibit a tradeoff between these desired thermal and mechanical properties. Compliant TIM materials such as thermal greases do not conduct heat as well as a solder joint. However, solder bonds result in high stresses that can cause device warping and cracking.

Vertically aligned carbon nanotube (VACNT) films have great promise as TIMs because they have high through-plane thermal conductance and mechanical compliance. These films also avoid drawbacks of polymer-based TIMs such as pump-out and drying. VACNT films are typically composed of a complex, entangled network of CNTs and the density and alignment of CNTs within a film affect its mechanical and thermal properties. Given the variety of growth techniques and variations in film morphology, it is important to understand how these factors influence film behavior.

The present work combines three major aspects of VACNT film characterization: mechanical and thermal characterization, analysis of the film microstructure, and modeling of the film properties. The combination of these is critical to understanding the relevant behavior of VACNT films for TIM applications. This will also help explain the large variation in past measured data, inform growth

techniques, and allow predictions of thermal or mechanical behavior based on film morphology.

The inhomogeneous VACNT film morphology is investigated by using image analysis to quantify CNT alignment and density and by measuring the elastic modulus at the top and bottom film surfaces using nanoindentation. The alignment and density information is input into a model of the mechanical response of the VACNT film, which is compared to measured data.

The through-plane thermal properties of VACNT films are measured using thermoreflectance techniques. Multiwall VACNT films are grown directly on a thermoelectric material and the thermal properties of the films are characterized using nanosecond thermoreflectance. A set of eight single-wall VACNT films are measured using frequency domain thermoreflectance to extract four relevant thermal properties: thermal conductivity, heat capacity, and the upper and lower boundary resistances.

Acknowledgements

I would like to thank my advisor, Professor Ken Goodson, for his guidance and support during my time at Stanford. He kept me motivated, let me pursue my own ideas, and helped me overcome many obstacles. I thank Professor Thomas Kenny for his support throughout my Ph.D. and for serving on my reading committee. Professor Wei Cai has helped tremendously with the mechanical property portions of my research and I thank him for his help and for serving on my reading committee.

The success of this research rested on the generosity of our group's collaborators. I would like to thank Senyo Dogbe and Dr. Lawrence Pan (Monano, Inc.) for providing me with some of my first CNT samples. Senyo worked with us closely throughout my Ph.D. in overcoming many challenges in nanotube growth. I'm very grateful to Professor Shigeo Maruyama, Professor Rong Xiang, Dr. Eric Einarsson and other members of the Maruyama group who have worked with the Goodson group for many years and provided many excellent samples. I thank Professor Brian Wardle (MIT), Dr. Scott Gilje (Northrop Grumman), Dr. Younez Ezzahri and Professor Ali Shakouri (formerly at UC Santa Cruz) and many others for their willingness to collaborate and provide samples.

I thank the senior members of the Goodson group: Matthew Panzer, John Reifenberg, and Jeremy Rowlette for teaching and mentoring me in my first few years at Stanford. I feel lucky to have worked closely with labmates Saniya LeBlanc, Amy Marconnet, Yoonjin Won, Takashi Kodama, and Michael Barako. They are wonderful people and amazing researchers and I'm very grateful for their support. I'd also like to

Table of Contents

List of Tables

List of Figures

xiv

xv

Chapter 1   Introduction

1.1   Overview of Thermal Interface Challenges

Thermal engineers are facing ever-increasing challenges in the modern world. This is fueled in part by the rapidly increasing power density of electronics. This not only includes the well-known rise of transistor density in processors but also includes other expanding fields such as cooling of LED lighting and datacenter operation. The physical size of mobile electronic devices such as phones, laptops, and tablets are continually shrinking while their computing power and pervasiveness are growing. This presents a severe thermal challenge in that fans used for forced convection are limited in size or cannot be used at all. Thermal management has become an integral part of the design process.

Interfaces at the joints between two materials in the heat conduction path can significantly hinder heat removal from devices. At an interface between two seemingly flat surfaces, only around 1-2% of the surfaces are actually in contact due to their microscopic roughness [1]. The situation is often exacerbated by the presence of ridges and non-planar surfaces which create large air gaps. This results in a huge thermal resistance because air is an extremely poor conductor with a thermal conductivity (k) of 0.01 W m^{-1} K^{-1}. The air gaps at interfaces must be filled with a thermal interface material (TIM) that conducts well thermally and conforms to the roughness of the contacting materials, as shown in Figure 1-1a. In the face of rising challenges in thermal engineering, there is strong demand for improving the thermal conductivity and reliability of thermal interface materials.

TIMs have traditionally been developed for the interface between a microprocessor and heat sink, shown in Figure 1-1b. Microprocessors can generate a significant amount of heat which must be dissipated to the ambient air through the use of a heat sink. The silicon chip is covered by a metal case which protects the chip and acts as a heat spreader. A thermal interface material enhances heat transfer between the case and heat sink. According to Fourier's law,

$$q'' = -k \frac{dT}{dx},$$

$$(1-1)$$

the heat flux (q'') through a material depends on k and the temperature change over a given distance (dT/dx). This leads to a definition of the thermal resistance of a material $R'' = L/k$ where L is the thickness of the material in the direction of heat flow. Figure 1-1b shows how each layer poses as a resistance to heat flow. In the thermal circuit analogy, q'' represents current and T represents voltage, giving the relationship $\Delta T = q'' \times R''$. To minimize the temperature difference between the chip temperature, T_{chip}, and ambient temperature, $T_{ambient}$, for a given q'', each resistance in the path of heat flow must be minimized.

If the heat sink and case are optimized, the TIM can become a bottleneck to device performance. The resistance of the TIM will depend on the TIM thickness, also called the bond line thickness (BLT), and k. For example, for a device dissipating 400W over an area of 6 cm^2, an average-performance TIM with $k = 3$ W m^{-1} K^{-1} and BLT of 30 μm would experience a temperature drop of ~6.7 °C. A high performance TIM at 100 W m^{-1} K^{-1} would reduce this temperature drop to ~0.2 °C, which means a decrease in chip operating temperature of ~6.5 °C. With devices being pushed to the limits of their recommended operating temperatures, every degree matters.

(a)

(b)
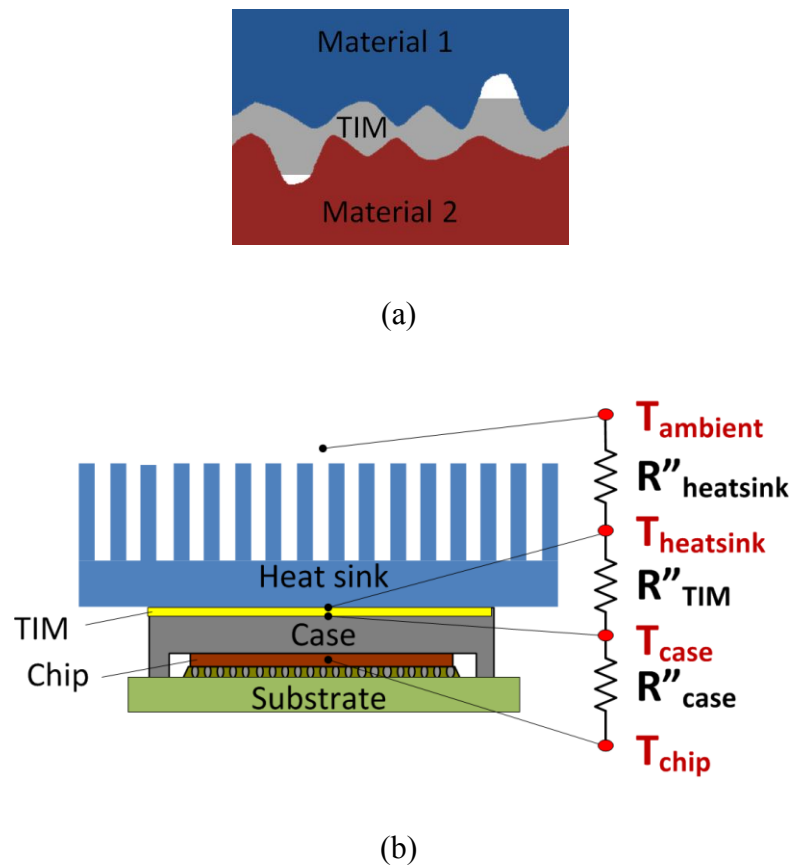
Figure 1-1: (a) A TIM joining two solid materials by conforming to the contours of the surfaces. Poor contact between the TIM and surrounding materials can create air pockets (the white regions), which hinder heat conduction. (b) Schematic of a heat sink pressed against a microprocessor chip which is encased by a metal lid and substrate. The TIM enhances thermal conduction between the case and heat sink. The thermal path between the microprocessor and ambient air is represented by a thermal resistance circuit.

Besides thermal conductivity, the mechanical properties of a TIM are also vital to its performance. Thermal interfaces usually join two different materials with different coefficients of thermal expansion (CTE). As the device temperature rises and falls during operation the TIM must be flexible enough to accommodate the resulting shear stress. If the two materials are bonded together with a stiff TIM such as a solder or epoxy, there can be warping, delamination, or cracking. This leads to reliability

3

issues which ultimately result in device failure. The maximum shear stress σ experienced by an interface material can be estimated using

$$\sigma = \Delta T(\alpha_1 - \alpha_2)\frac{GL}{2d},$$ (1-2)

where ΔT is the temperature excursion from the zero stress condition, α_1 and α_2 are the thermal expansion coefficients of the substrates, G is the shear modulus of the TIM, L is the joint length, and d is the BLT [2]. This equation assumes that the TIM is relatively thick and flexible, and that the substrates are unyielding. This equation gives an upper bound of the stress because it does not account for the strain capabilities of the materials.

Many commercial TIMs exhibit a tradeoff between high k and low mechanical modulus because this material combination is not typical of natural materials. For example, soft materials such as polymers are not efficient heat conductors, but conducting materials such as metals are stiff. Examples of commercial TIMs are listed in Table 1. Additionally, there are other important considerations in TIM design such as reliability, cost, and ease of application. Thermal greases, the cheapest and most commonly used TIM, are difficult to apply, contain air pockets, and require high clamping pressures. Even worse, many TIMs tend to degrade over time as they get squeezed out, dry up, or degrade from high temperatures and thermal cycling. There exist hundreds of brands of TIMs but improvements over the years have been marginal.

Nanostructured materials are promising as TIMs because they provide properties not found in nature. These include carbon-based TIMs and composites, based on carbon nanotubes (CNTs), graphite, and carbon fibers [1, 3]. The unique structure of these carbon-based materials gives them high flexibility and thermal conductivity. Many forms of these TIMs have been commercialized, most as

4

composites. This work focuses on vertically aligned carbon nanotube TIMs, which are introduced and discussed in the next section.

Table 1-1: Commercial TIM advantages and disadvantages, adapted from [1, 3].

TIM Type	k (W m^{-1} K^{-1})	Advantages	Disadvantages
Greases	3-9	• Fills in voids • No delamination • Low cost	• Not uniform • Pump-out • Dries out • Messy
Phase change materials	4	• Less pump-out • No delamination • No dry-out	• High attachment pressure, higher stress • Voiding
Adhesive (tape, epoxies)	0.7 - 1	• Easy to apply • Conformal • No pump-out/migration	• Low k • Delamination • Stiff
Solders	50	• High k	• Voiding • Cost & complexity • Stiff

1.2   Introduction to Carbon Nanotubes and Vertically Aligned Carbon Nanotube Films

CNTs have been the subject of intense research over the past few years due to their extraordinary thermal, mechanical, and electrical properties. CNTs can be described as rolled-up sheets of graphene, which consists of a one-atom-thick layer of hexagonally-arranged sp^2 bonded carbon atoms. This unique molecular structure gives CNTs their exceptional properties. Figure 1-2 illustrates two types of CNTs. A single-wall nanotube (SWCNT) consists of one tube and has a diameter of around 2 nm. A multiwalled nanotube (MWCNT) consists of multiple concentric tubes and their diameters can range from a few nanometers to hundreds of nanometers.
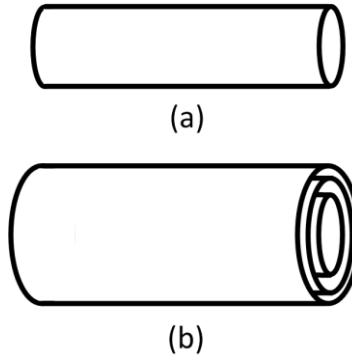
Figure 1-2: (a) Schematic of a SWCNT consisting of a tube with walls of graphene. (b) Schematic of a MWCNT with three walls and a larger radius.

CNTs have been shown to have extremely high k in their axial direction, with most measurements reporting k ~3000 W m^{-1} K^{-1} [4-7]. This is about an order of magnitude higher than the conductivities of Cu and Ag which have k ~400 W m^{-1} K^{-1}. This combination of conductivity and flexibility makes them extremely attractive for TIM applications.

As TIMs, a dense array of CNT aligned in the direction of heat flow represents the ideal configuration that takes advantage of their axial thermal conductivity and flexibility. A promising method to manufacture such a material is growth of vertically aligned "forests" of nanotubes. The as-grown CNT volume fraction, f, is typically around 10%. Though this may seem low, if the CNT individual conductivity of $k =$ 3000 W m^{-1} K^{-1} is scaled by f, the effective conductivity of the film is potentially as high as 300 W m^{-1} K^{-1}, an order of magnitude higher than solder. While individual nanotubes are known to have a high stiffness, characterization of arrays of nanotubes has shown a comparatively low axial elastic modulus due to the low packing density of the CNT array and large aspect ratio of individual tubes [8]. CNT arrays can currently be grown up to millimeters in height and over large areas to accommodate a wide range of interface geometries [9]. Besides being thermally conducting and flexible, vertically aligned CNT (VACNT) TIMs also have the advantages of being

6

dry and reliable. Because the film can be grown to several millimeters in height, it is useful for applications with large or varying gap sizes as well.

One common way to fabricate VACNT films is through chemical vapor deposition, in which aligned nanotubes form from the reaction between catalyst particles on a substrate and the carbon-containing gas flowing over the substrate. There exist many variations of growth methods and each one produces a slightly different CNT morphology. Some methods produce VACNT films with low f and perfectly aligned, large diameter tubes. Others produce disordered "mats" of CNTs. The growth methods of the films in this work are detailed in the later chapters and references. Figure 1-3 shows scanning electron micrographs (SEMs) of a VACNT film similar to the films measured in this study. The first image shows a 100 μm-thick film that appears dense, with well-aligned CNTs. However, upon closer inspection these CNTs are not perfectly straight, as shown in Figure 1-3b. Zooming in further in Figure 1-3c, it becomes evident that the film has a sponge-like structure, with gaps between tubes about 100-200 nm wide. Figure 1-3d illustrates nanoscale tube-tube crossing and bundling behavior, along with the hexagonal arrangement of the carbon atoms which form the tube walls. Bundling is due to van der Waals forces and contributes to the film's complex structure.
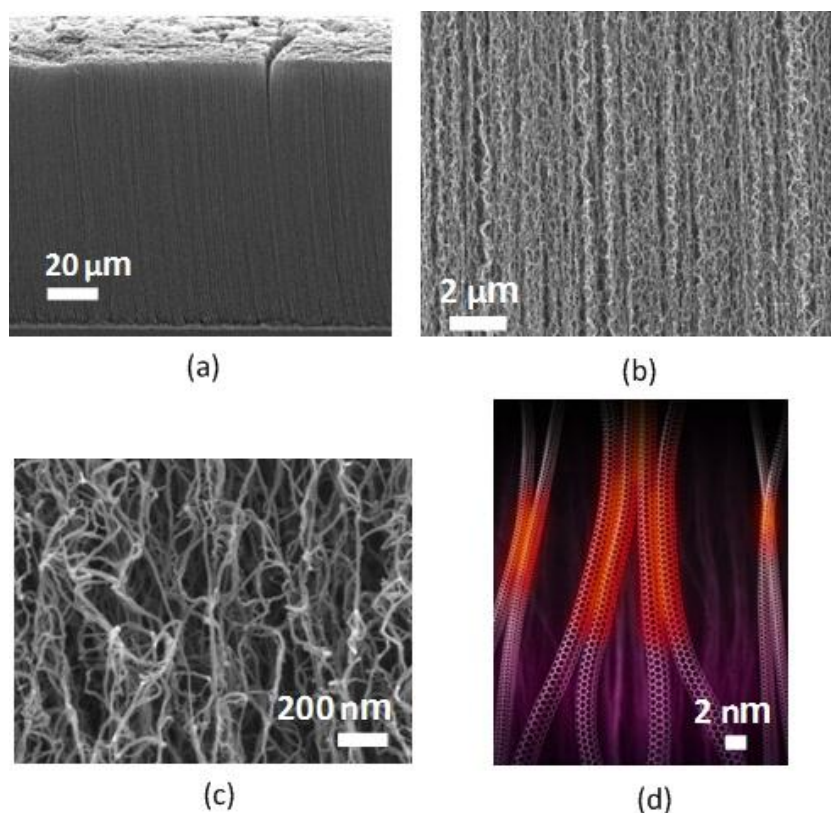
Figure 1-3: (a) Cross-sectional SEM of a 100 μm-thick VACNT film. (b) SEM image of a region near the center of the film. (c) High magnification SEM showing the entangled CNT structure. (d) A rendered graphic depicting several SWCNTs bundling and crossing. Image courtesy of Alex Jerez and Yoonjin Won.

It is often challenging to characterize nanostructured materials and CNTs are no exception. There are three main aspects to characterizing VACNT films. There have been past work in each of these that are referenced in the later chapters.

The first is the measurement of film properties. Though there have been extensive mechanical, thermal, and electrical measurements of individual CNT properties, such properties of VACNT films are not well understood. There have been a number of measurements of either mechanical or thermal properties of VACNT films. However, the past data are scattered and span several orders of magnitude.

Much of the film thermal conductivity data falls far below expected values based on individual tube measurements.

The second aspect is quantifying and understanding the microstructure of the CNTs in the film. The structure, such as CNT alignment, density, CNT radius, and presence of impurities, can affect the film's physical properties and can vary significantly between films. This characterization is challenging due to the complex inhomogeneous morphology of the film. Past work has involved analyzing the film morphology using a microscope or other techniques such as Raman spectroscopy to measure alignment and density. These values are rarely reported with thermal and mechanical property measurements.

The third aspect is modeling of film properties. Models should include structural parameters such as film density, alignment, and thickness to simulate thermal or mechanical properties. Individual CNTs have been simulated using molecular models to observe effects such as radius, length, and defects. There is yet no effective method to simulate the entire film. One challenge in creating accurate models of films is in understanding the effects of the film's microstructure. For example, the effect of tube-tube bundling on thermal and mechanical behavior and the amount of bundling are hard to determine. Ideally the model and data are compared by varying one film property at a time over a large set of samples but there is often limited control and knowledge of the many variables in a film for accurate comparison to simulations. Most published work measure only a few samples at a time.

Addressing these points simultaneously serves several purposes. Quantifying the morphology of the film will help standardize and explain measured film properties. Understanding the relationship between film morphology and property data will inform growth experts on how to create a film with the desired properties. With appropriate models a film's physical properties can be calculated based on morphology data alone.

9

1.3   Scope of Work

This work aims to address the missing links between measurement, modeling, and morphology analysis of VACNT films. One goal of this work is measurement of thermal and mechanical properties of VACNT films since these are the most relevant properties for TIM applications. This includes setting up experimental tools to measure thermal conductivity, heat capacity, boundary resistances, and elastic modulus. This work also includes investigation of VACNT TIMs for thermoelectric applications, which can have extreme operating conditions. Another goal is establishing a technique to quantify the structure of the film. This is done using image analysis of SEM images of the film structure. The last aspect of the work includes developing a mechanical model to predict mechanical behavior based on film morphology.

1.4   Organization

Chapter 2 presents the first measurements of the modulus of the top and base sides of multiwalled VACNT films. The base side has a more entangled morphology than the top side -- this measurement gives an opportunity to compare the effect of each on the modulus. The VACNT films are released from their substrates to access the base side. The experimental setup involves custom spherical indenter tips used with an atomic force microscope to perform nanoindentation measurements. An image analysis technique is introduced that quantifies the morphology of VACNT films. This image data is used in a model based on the behavior of foam materials which is then compared to the measured modulus.

Chapter 3 begins by introducing the reliability challenges of thermoelectric modules used in waste heat recovery applications. In particular the interfaces between the thermoelectric material and metal leads often experience high stresses that result in degradation of device performance. This chapter investigates replacement of that solder bond with a VACNT film. Multiwalled VACNT films are grown directly on a

thermoelectric material and the thermal properties are characterized using nanosecond thermoreflectance.

Chapter 4 investigates the thermal performance of a set of seven single-wall VACNT films. The thermal conductivity, heat capacity, and boundary resistances of the films are measured. To allow independent extraction of these four relevant thermal properties, a frequency-domain thermoreflectance measurement setup is developed and described here. The CNT alignment and density through the film thickness is also examined using relevant image data.

Chapter 5 summarizes the work presented and includes a discussion of future studies and improvements to VACNT films.

Chapter 2 Inhomogeneous Mechanical Properties of Multiwalled VACNT Films

2.1   Introduction

The thermal resistance and reliability of thermal interface materials (TIMs) are critical limiting factors for a variety of technologies including electronics thermal management and thermoelectric energy conversion [1, 10]. Vertically aligned carbon nanotube (VACNT) films offer great promise as TIMs because they offer high through-plane thermal conductance and mechanical compliance. VACNT films typically have a complex, entangled nanotube structure and morphological details such as the density, alignment, and tortuosity of CNTs within a film affect its mechanical and thermal properties. Given the variety of growth techniques and variations in film morphology, it is important to understand how these factors influence their behavior as TIMs. VACNT films will need to be released from their growth substrate and attached to the device being cooled, so released films must also be characterized.

While there has been considerable work on measuring the thermal performance of VACNT films [11, 12], the mechanical properties need more attention. Past research on the mechanical properties of VACNT films yielded a wide variety of out-of-plane modulus (E_2) values ranging from below 10 MPa to hundreds of MPa [13-21], likely due to the variety of film structures and measurement techniques. Prior work often assumed that the film structure is homogeneous, which is in contrast with the strongly varying in-plane modulus (E_1) we reported recently for multi-walled VACNT films of thicknesses between 0.5 to 100 μm [22] based on both SEM images

and thickness-dependent modulus data obtained using a novel resonator technique. This suggests that understanding and quantifying the inhomogeneous morphology of VACNT films in conjunction with elastic modulus measurements will improve data interpretation and analysis.

Several studies quantifying the morphology of VACNT films and mats using image analysis or X-ray diffraction showed that the structure varies strongly with height [23-25]. There is often a thin, highly-entangled crust layer, followed by a more vertically aligned middle section, which is then followed by a disordered, lower density base region. The distinction between these regions tends to be more pronounced for films much thicker than 10 μm [24]. Some studies observed a relationship between the tortuosity of VACNT films and measured modulus [15, 26, 27], while others observed that buckling always begins at the film base during uniform compression [16, 18-20, 28, 29]. These studies indicate that the film microstructure strongly influences the mechanical properties of the film. However, none of these use quantitative microstructure analysis of the film to predict mechanical behavior.

The present work extracts the localized out-of-plane mechanical modulus of five multi-walled VACNT films with thicknesses ranging from 98 to 1300 μm through nanoindentation by an atomic force microscope (AFM). Previous work used AFM nanoindentation on a well-aligned CNT film to measure individual CNT properties by using a sharp pyramidal tip to penetrate between the tubes [30]. Instead, we use spherical indenter tips with radii between 15 and 25 μm to measure bulk behavior rather than individual tubes. We measure the differences in E_2 between the top and bottom regions, which often have different morphologies. The modulus on the top side ($E_{2,top}$) is performed on as-grown films. The modulus at the bottom surface ($E_{2,base}$) is measured by releasing the film from the substrate and indenting from the backside. In this way we can observe the inhomogeneous mechanical behavior within VACNT films and compare the results between films of different thicknesses. Image analysis performed on SEMs of the samples quantifies their alignment and density. These

13

values are input into a cellular mechanical model to relate calculated behavior to measurement results. This allows prediction of a film's mechanical properties from image data alone. Much of this work was previously published in Gao *et al.* [31].

2.2 Experimental

2.2.1 MATERIAL PREPARATION

This work investigates five multi-walled VACNT films grown under similar conditions with final film thicknesses of 98, 150, 200, 205, and 1300 μm. The growth process and density measurement procedures are detailed in Won et al. [22]. The mass densities range from 0.029 to 0.056 g cm^{-3} which translates to 1.3% to 2.5% volume fraction (*f*) assuming an individual multi-walled CNT density near graphite of 2.2 g cm^{-3}. To indent the films on the base side, the VACNT films are released from the substrate by first placing the top of the film on a thin layer of carbon paste (Structure Probe, Inc.) on a second substrate and then pulling the original substrate off after the adhesive dries (Figure 2-1a). Carbon paste is used for this study because it is SEM compatible and easy to apply- in actual TIM applications, the film can be bonded and released with a binder metal to enhance thermal conduction [32]. The carbon paste is viscous and there is little wicking into the film. To avoid changing the film's microstructure, minimal pressure is applied when bonding the film. Each released sample is inspected under SEM and samples with significant damage are not used in the study. Figure 2-1b and c illustrates the indentation of the original film and flipped film respectively.

Figure 2-1d shows an SEM image of an indenter consisting of a 25 μm diameter glass microsphere (Polysciences, Inc.) attached to the end of a tapping-mode AFM cantilever (TAP-190AL-G, BudgetSensors). Three different indenter tips are used in this study with spheres of radii 15, 20, and 25 μm determined using SEM images. The large diameter ensures sampling of bulk film properties rather than individual nanotubes. Tubes are typically spaced ~100 nm apart and a sharp AFM tip

will penetrate the surface and push tubes laterally. Unlike sharp indenters the large radius also allows accurate determination of the tip geometry for the force curve analysis. Compared with flat indenters the spherical probe does not need to be aligned perfectly perpendicular to the surface of the sample. The glass indenter tip (E ~70 GPa) is much stiffer than the films being investigated (E < 10 MPa).
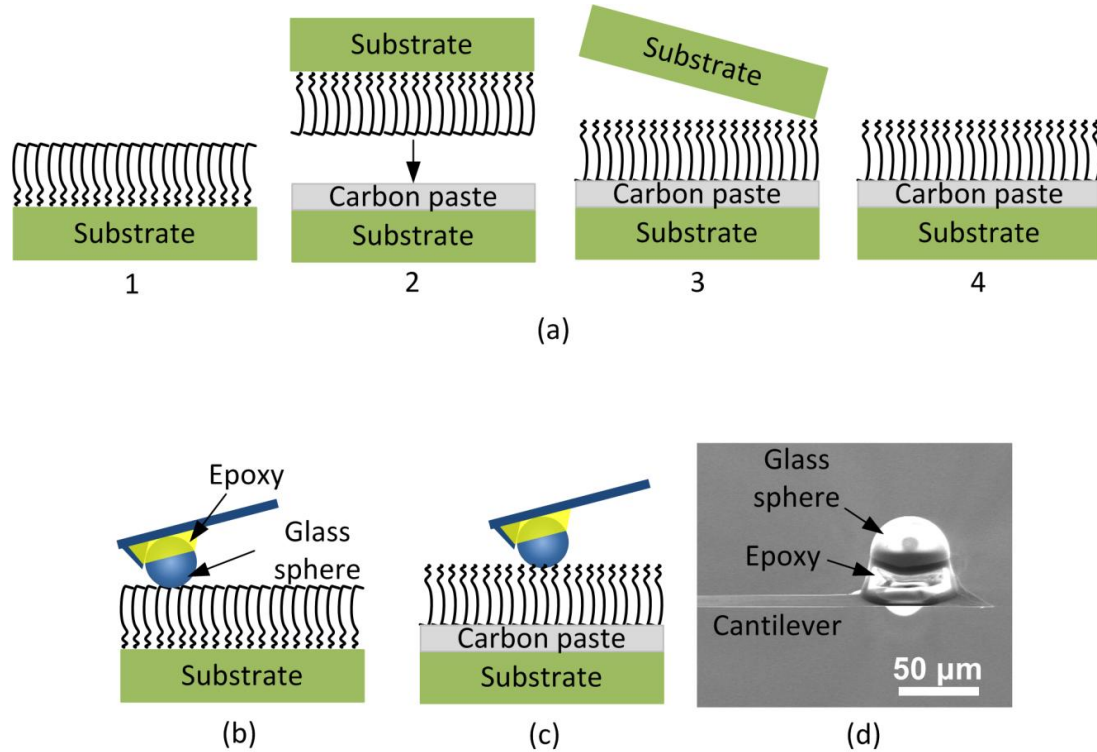
Figure 2-1: (a) Schematic of the VACNT film release procedure for measurements of the base side modulus. 1. The as-grown VACNT film. The array of curvy lines represent the VACNT film with a crust layer and wavy base side. 2. The top of the original film is bonded to a new substrate using carbon paste. 3. The original substrate is pulled off after the carbon paste is dry. 4. The final, flipped film for base-side indentation. (b) Indentation of the top side of an as-grown film. (c) Indentation of the base surface of a VACNT film that has been bonded to a new substrate. (d) SEM of the indenter tip. The original AFM tip which is nominally 17 µm tall is located to the right of the glass sphere and is partially covered with epoxy. The white shadows in the image are due to charging effects during imaging.

The spring constant κ of each cantilever is calculated using the Sader method [33] before attachment of the glass spheres. For this calculation a laser Doppler vibrometer is used to find the quality factor and resonant frequency of each AFM cantilever and the cantilever width and length are measured using SEM images. The measured κ values range from 17 to 20 N/m. The glass spheres are first cleaned using a Piranha solution to remove surface residue. Then spheres are attached with epoxy to each cantilever based on the method described in Kodama et al. [34].

2.2.2 MEASUREMENT METHODS

The goal of this work is to extract the local, out-of-plane modulus at the top and bottom surfaces of VACNT films. VACNT films with entangled morphologies have been shown to behave as a foam-like network of tubes rather than independent, vertical CNTs since there are significant tube-tube interactions due to van der Waals forces [13, 15, 16, 19, 20, 24]. To measure localized properties at the top and base regions, a nanoindentation technique is used to indent a small, shallow region of the film. The stress field due to the indenter is typically localized to the region below the indenter. This is in contrast to previous uniaxial compressions of VACNT films with minimal lateral forces [16, 18-20, 28, 29]. In those measurements the film essentially acts as a series of vertical springs and the weakest layer (typically the base) deforms the most regardless of the direction of indentation.

The elastic modulus of each VACNT film in this work is measured using a Topometrix Explorer scanning probe microscope capable of force measurements. These microscopes provide high sensitivity to load and displacement and have been previously used to measure the mechanical properties of a variety of materials, including polymers and biological materials, yielding information about local material properties such as hardness, elasticity, and adhesion [35, 36]. AFMs are especially

useful for observing soft, fragile samples and allows for use of a variety of indenter sizes, materials, and cantilevers.

To obtain an accurate load-depth curve a number of calibration and conversion steps are performed. The piezoactuator is calibrated to account for nonlinearity, hysteresis, and creep between the applied voltage and displacement [37]. For each measurement, the conversion of photodiode voltage to cantilever free-end deflection is determined by pressing the tip on a hard sample such that there is no penetration into the sample. The cantilever deflection is converted to force F using $F = \kappa \times x$ where x is the cantilever deflection. Because the loading force is affected by the tilt of the AFM cantilever with respect to the sample, a correction factor given in Heim et al. [38] is applied which also accounts for indenter size. During the measurement the tip deflection is kept within the linear region of the photodetector. The data are taken using a tip velocity of 4 μm/s, which is sufficiently fast to render the data independent of velocity. The actual load signal resolution depends on the range of indentation and number of data points taken but remains below 20 nm in displacement and 8 nN in force.

The Young's modulus of the material can be determined from the load-depth curve using the Oliver-Pharr method [39], which is appropriate for elastic-plastic materials and has been previously used on other measurements of VACNT films which exhibit this behavior [14-16]. The slope of the initial unloading curve, S, represents purely elastic recovery and is a measure of the contact stiffness $S = dP/dh$ where P is the load and h is the displacement. To find S, the initial portion of the unloading curve is fit to a power law relation. S is related to the reduced modulus E_r by

$$E_r = \frac{S}{2} \frac{1}{\sqrt{2h_c R_i - h_c^2}}$$

(2-1)

17

where R_i is the radius of the indenter and h_c is the actual contact depth given by

$$h_c = h_{max} - e\frac{P_{max}}{S}.$$ (2-2)

Here h_{max} is the total indentation depth below the surface of the film and e is a geometrical constant equal to 0.75 for a paraboloid of revolution. The initial contact point is determined from the point where the force curve deviates from the zero force line. There is some error in choosing the location of this contact point, but the results are not strongly sensitive to h_{max}. The modulus of the film is calculated from E_r using

$$E_r = \left[\frac{1-v_i^2}{E_i} + \frac{1-v_f^2}{E_f}\right]^{-1},$$ (2-3)

where E_i, v_i, and E_f, v_f represent the Young's modulus and Poisson's ratio of the indenter (glass sphere) and substrate (VACNT film), respectively. The values of E_i and v_i used for glass are 70 GPa and 0.2, respectively. The value of v_f for VACNT films is commonly assumed to be zero because the response is similar to a foam material [16, 19].

The Oliver-Pharr method does not include adhesion effects, which are significant for measurements on the base of the film and can yield error in the analysis [40]. The top surface may have lower adhesion than the base due to the entangled crust layer, which reduces engagement of the CNTs to the contacting surface [21, 41]. Thus data for the base of the film are also analyzed using Johnson-Kendall-Roberts (JKR) adhesion theory [42]. According to the Tabor parameter, the JKR model is valid for these samples, which are compliant, elastic materials with high surface energy and measured with large radii indenters [43]. Fitting the force curve to the model gives E_2 and the work of adhesion $\gamma = 2P_{adh}/(3\pi R_i)$ of the sample, where P_{adh} is the maximum adhesion force [40].

18

The inhomogeneous and anisotropic morphology and surface roughness of a VACNT film poses many challenges for nanoindentation measurements. Theory accounting for these effects is often complex and may be different between foam materials and dense solids. These effects are discussed below.

Because the samples are porous, they have high surface roughness -- on the order of 100 nm and 1 μm root mean square roughness for the top and base respectively based on AFM topography scans. The roughness may be lower for the top because of the horizontally-aligned tubes in the crust layer, whereas the released base consists of vertical CNT tips. Past work showed that roughness results in an underestimated modulus and scattered data, and that its effects diminish with indentation depth [44, 45]. Errors due to roughness are mitigated by averaging results from different locations and indenting deeper than the surface roughness. Measurements are taken on each sample using at least two different indenter tips and at least five different locations for each tip for a total of over 10 indentations per sample. Measurements are not repeated at the same location due to the stress softening behavior of the film [18, 46]. The average indentation depth for the samples ranges from 600 - 1160 nm for the top surface and 2.17 - 6.62 μm for the base, corresponding to 0.09–0.80% strain for the top and 0.3–3.0% strain for the base. A schematic illustrating the relative scales of indentation depth compared to the thickness of each region in a VACNT film is shown in Figure 2-2. Based on image data, the CNT alignment in a film actually changes gradually, so the thicknesses of the "Top" and "Base" regions are approximate.
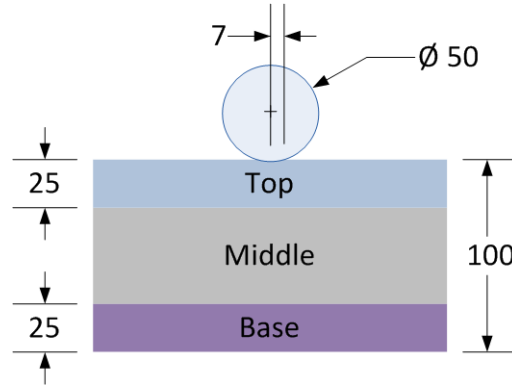
Figure 2-2: Diagram of indentation depth and regions in a 100 μm-thick VACNT film drawn with relative dimensions approximately to scale. Units are in microns. The approximate contact radius of 7 μm corresponds to the maximum indentation depth at the top surface.

Indentation of rough surfaces can be divided into two steps. There is first flattening of the asperities, then indentation of the flattened surface [47]. As shown in Figure 2-5, the "free" tips of the base-side nanotubes deform plastically to form a flattened surface against the indenter tip, creating a profile similar to a crust layer. During applied load the base side experiences a greater increase in CNT-indenter contact area than the top, which may lead to greater underestimation of $E_{2,base}$ than $E_{2,top}$. Because we cannot observe the progression of contact area during indentation, we estimate this effect by changing the initial contact point in the analysis such that the loading begins after the flattening of the base side tips. This reflects the extreme case of no contact before this point, simulating extremely sparse CNT tips. For a 20% lower h_{max}, E_2 calculated using the Oliver-Pharr method increases proportionally by 20%. However, E_2 calculated using the JKR method only increases by 3%. Thus the deep indentations and JKR analysis reduce the underestimation of $E_{2,base}$.

To achieve a localized measurement, the nanoindentation measurement must not sample the layers below the region of interest. In indentation of multilayer substrates, the measured modulus is dictated by the ratio of contact radius to layer

thickness (a/t) [48-50]. This results in a measured modulus that varies with penetration depth, in which the modulus approaches that of the sub-layer for an a/t ratio of 10 or higher. Thus for VACNT films, the top side indentation would progressively sample the top, middle, then base layer. Because VACNT alignment is in fact gradually changing with depth, the measured moduli are an average of the local properties at the top and base. Indentations must be kept shallow to keep a/t below 10 and there should be minimal change in modulus with depth. Some indentations at the base side are deeper than this, which would cause an overestimated $E_{2,base}$ due to the higher modulus of the middle layer.

There is also some lateral spreading of the stress field during nanoindentation, which means the measurement is not purely sampling E_2. The VACNT film is transversely isotropic and E_1 is expected to be much lower than E_2. The higher the anisotropy, the greater the underestimation of E_2. If the top is more aligned than the base, $E_{2,top}$ will experience greater underestimation. Extracting these components of the modulus involves complex analysis that requires knowledge of the full stiffness matrix and indenter geometry [51, 52]. This analysis and measurement of all the elastic constants of the film is beyond the scope of this work, but the effects of anisotropy can be estimated. Vlassak $et\ al.$ showed that an anisotropy factor of 10 and Poisson's ratio of 0.3 can result in measured modulus about 50% lower than the actual E_2 for a crystal [51]. A lower Poisson's ratio, as in foams, should further limit the lateral spreading of stress. The measured modulus also depends on the indenter shape. For a flat indenter, the measured value is close to the modulus in the indentation direction, while a sharp tip is more sensitive to the properties of the in-plane direction [53]. A larger spherical indenter gives a flatter contact area that provides higher sensitivity to the out-of-plane modulus.

In summary, the measured response depends on indenter geometry (size and shape) and indentation depth. There is no significant difference in measurement results between tips, indicating that the measured results are not highly sensitive to the tip

radius. Indentations should be deeper than the surface roughness but not deep enough to sample the middle layer, and large radius indenters are desired to reduce lateral strain because the film is anisotropic. The surface roughness may result in underestimation of $E_{2,base}$ while sampling of the middle layer can lead to overestimated $E_{2,base}$. Anisotropy primarily results in underestimated $E_{2,top}$, which emphasizes the difference in modulus between the top and base.

The measurement system is verified using a 1 mm-thick polydimethylsiloxane (PDMS) 10:1 reference sample (Sylgard 184, Dow Corning Inc.). The Poisson ratio of PDMS is assumed to be 0.5. The measured modulus values are 1.3 ± 0.2 MPa which match well to past work that reported ~1.5 MPa elastic modulus [54, 55].

2.2.3 CELLULAR MODEL

Past literature has shown that the mechanical response and microstructure of VACNT films can be effectively modeled as an open-cell foam [18, 19]. Open-cell foams have been previously analyzed using dimensional relations between the mechanical modulus and a measure of the physical structure (*e.g.*, unit cell size) because the variation in pore size and geometry makes it difficult to create an exact model. These relations have excellent fit to data down to a constant of proportionality [56]. For this analysis we use a simple three-dimensional open-cell foam model similar to the work of Gibson et al. [56] to simulate the mechanical response of the VACNT foam using dimensional relations.

Figure 2-3a shows a unit cell comprised of eight CNT sections of length l oriented at an angle θ to the plane of the film. The unit cell has height H and length and width L to account for modulus anisotropy between the CNT growth direction (out-of-plane) and in-plane directions. The aspect ratio α is defined as $\alpha = H/L = \sqrt{2}\tan\theta$. Figure 2-3b shows a single angled tube segment from which the relationships $H = 2l\sin\theta$ and $L = \sqrt{2}l\cos\theta$ are derived. The cellular model does not capture the variety of complex tube interactions such as tube-tube bundling and

22

van der Waals forces in the structure, but the results of this model match well to a coarse-grained molecular simulation of the film structure that does account for those effects over a wide range of α and f [1].

The present analysis assumes that the VACNTs act as Euler-Bernoulli beams. For E_1, a horizontal force F_1 is applied at the end of each beam and for E_2, a vertical force F_2 is applied at the end of each beam (shown in Fig. 2b). The resulting in-plane and out-of-plane strains ε_1 and ε_2 are

$$\varepsilon_1 = \frac{\Delta_1}{L/2} \propto \frac{F_1 l^3 (2 - \cos^2 \theta)}{E_s I L} \tag{2-4}$$

$$\varepsilon_2 = \frac{\Delta_2}{H/2} \propto \frac{F_2 l^3 \cos^2 \theta}{E_s I H} . \tag{2-5}$$

Here Δ_1 and Δ_2 are the beam deflections in the in-plane and out-of-plane directions respectively. I is the principal moment of inertia. $I = \pi (R_{out}^4 - R_{in}^4)/4$ where R_{out} is the outer radius of a CNT and R_{in} is the inner radius. E_s is the Young's modulus of an individual CNT, which is typically ~1 TPa [57]. The total stress on the cell in the in-plane direction, σ_1, and out-of-plane direction, σ_2, is $4F_1/LH$ and $4F_2/L^2$, respectively.

[1] Won Y, Gao Y, Panzer MA, Goodson KE. Zipping, Entanglement, and the Modulus of Aligned Single-Walled Carbon Nanotube Films. Unpublished. 2012.
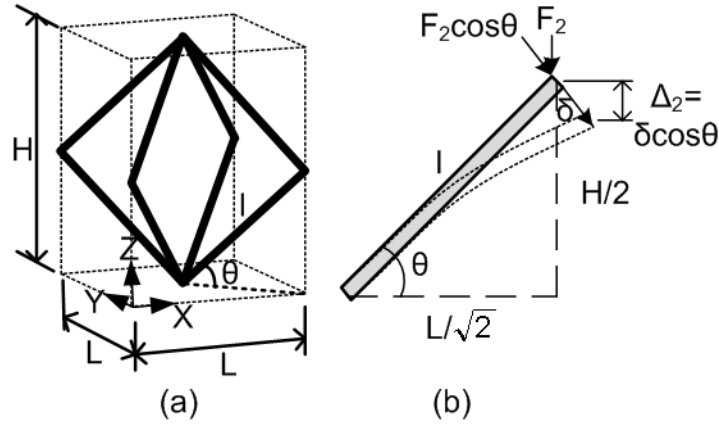
Figure 2-3: (a) Anisotropic unit cell where $H > L$. H is the growth (out-of-plane) direction. The nanotubes are hollow cylinders represented by the thick solid lines of length l. (b) Diagram of a single tube with a vertical force F_2. The beam is deflected by Δ_2 in the vertical direction.

The volume fraction f can be expressed as the relative volume occupied by the nanotubes in a unit cell.

$$f = \frac{8lA}{L^2 H} = \frac{2A}{l^2 \cos^2 \theta \sin \theta} \quad . \tag{2-6}$$

Here A is the cross-sectional area of an individual CNT. After substituting l with f in Eq. 2-4 & 2-5, E_1 and E_2 become a functions of θ, f, and individual tube properties:

$$E_1 = \frac{B \cos^4 \theta \sin \theta}{2 - \cos^2 \theta} \tag{2-7}$$

$$E_2 = B \sin^3 \theta \tag{2-8}$$

$$B = \frac{CE_s I f^2}{A^2} \quad . \tag{2-9}$$

The values of f and α (where $\alpha = \sqrt{2}\tan\theta$) are calculated for each indented region using the image analysis procedure described in the next section. B is defined to factor out the dependence on f, because each region of the VACNT film has a different α and f -- this allows isolation of E_2 dependence on α. The measured E_2 are converted to a relative modulus $E_{2,rel} = E_2/B$. Then $E_{2,rel}$ is compared to the predicted trend, $\sin^3\theta$ (Eq. 8 divided by B). Because these are dimensional relationships, C is defined as a constant of proportionality which is determined by using a least squares fit between the data and model.

2.2.4 IMAGE ANALYSIS

Image analysis techniques are used to estimate H and L at various locations in a cross-sectional SEM image of the VACNT film to detect morphological variations. For image analysis, the VACNT samples are first cleaved to gain visual access to the nanotubes away from the sample edges. The cleaved edge is sputter coated with ~4 nm Au to increase SEM image contrast. The image analysis technique is insensitive to the tube diameters. All images of the film are taken using a FEI XL30 Sirion SEM at 150 kX magnification under identical microscope settings. This provides the best images for analysis in terms of capturing a large area with adequate resolution, as shown in Figure 2-4a, and keeps the depth of field constant. An image at this magnification covers roughly a 1.5×2 µm area.

Binarization of the SEM images using thresholding (the Otsu method) limits the image to a thin plane because brightness decreases with depth. Slight variations in threshold value do not have a significant effect on the results. If a large portion of the image is not in the same plane, that area is cropped out. Image processing operations are used to remove noise and large specks. An example of the final binary image is shown in Figure 2-4b. The intersections between the nanotubes and 50 evenly spaced probe lines are counted in both the horizontal and vertical directions, as in Figure 2-4c and d. This is a standard stereological procedure for quantifying geometries in a cross-sectional image [58], and the number of probe lines do not significantly affect the

results above a certain point. The average tube-tube spacing is calculated by dividing the total probe line length by the total number of intersections. The measured tube-tube distance in the horizontal and vertical directions are converted to 3D cell dimensions L and H using a factor of 1.5 [56] which are then converted to f and α using the cellular model. The factor gives the appropriate film f of ~2% as determined from the mass density measurements.
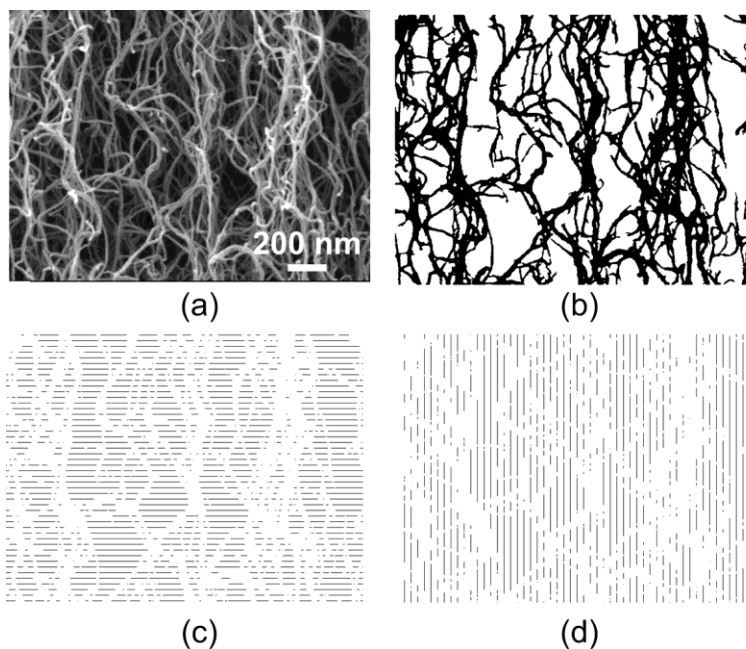
Figure 2-4: (a) An SEM is taken of a section of the VACNT film that is roughly in one plane. (b) The binary image after filtering. (c) Horizontal and (d) vertical straight probe lines drawn across the binary image to detect intersections with nanotubes.

2.3   Results and Discussion

The crust, top, middle, and base regions within a typical VACNT film are indicated in Figure 2-5a. Figure 2-5b shows the flipped film attached with carbon paste to a secondary substrate. Figure 2-5c shows the released surface with an indented region (see discussion of roughness, Section 2.2). The crust on the original film, shown in

26

Figure 2-5d, is ~200 nm thick for the films in this study, which is too thin to analyze reliably using the image analysis procedure. As discussed later this crust layer does not significantly affect the modulus measurement. The images used for analysis are taken immediately below the crust in the top region. Figure 2-5e and f depict the well-aligned middle and entangled base regions.
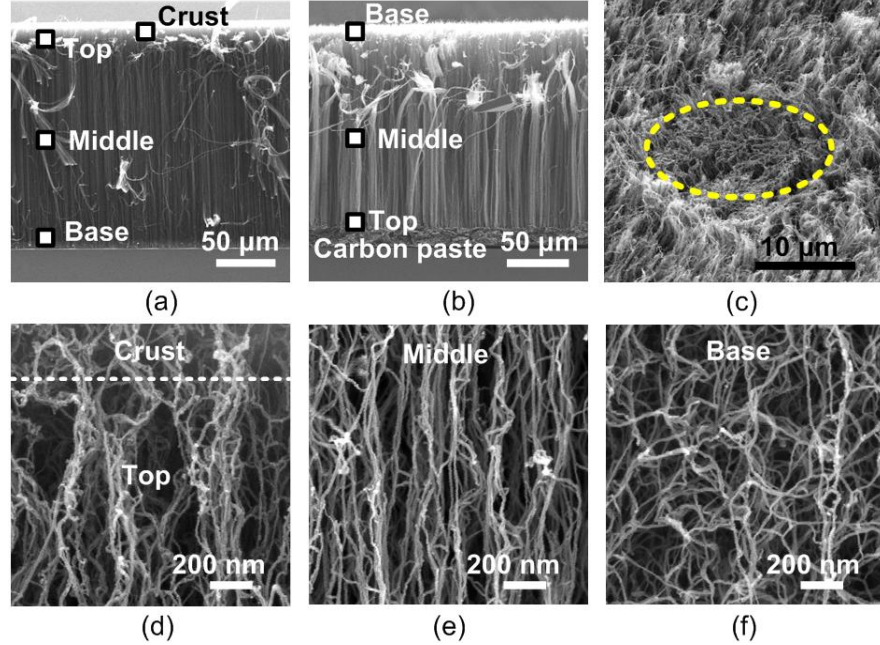
Figure 2-5: (a) Cross-sectional SEM of a 200 μm-thick VACNT film showing locations of the crust, top, middle, and base regions. The crust is directly above the top region. (b) The released and flipped film on carbon paste with the original regions reversed. (c) SEM image of a 45° view of a released base surface with a region of plastically deformed CNT tips (circled) from indentation. The released surface has no crust layer. (d) SEM images of the crust and top, (e) middle, and (f) base regions showing the differences in CNT morphology.

These trends are also reflected in Figure 2-6 which shows the quantified tube structure using the image analysis procedure. The result shows that α peaks in the middle region and tends to be lower at the base than the top. Similar trends exist for all the samples and are akin to past observations [24]. The values of f are more scattered,

27

partly because obtaining density information from SEM images is less accurate than the alignment due to the impact of the depth of field of the SEM.
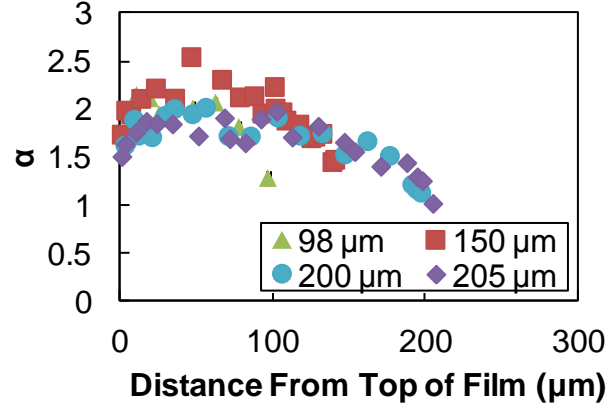
(a)
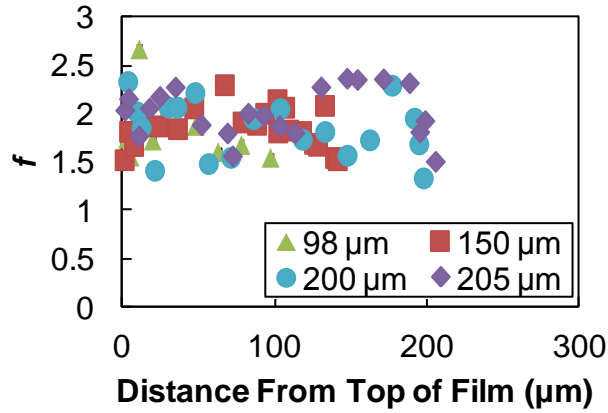
(b)

Figure 2-6: Image analysis results for the 150 μm-thick sample showing (a) α and (b) f calculated from SEM images as a function of depth into the sample. Zero distance corresponds to the top of the film. The 1,300 μm-thick sample is not shown for clarity. In each region, over all samples the standard deviation of α and f is between 3–12% and 5–18% respectively. These results are used as inputs to the cellular model.

The images of the released films are also analyzed to determine if the release procedure changes the film morphology. The morphology of the flipped films matches the original film within the scatter of the data. For comparison to measured data, at least three images are taken at the top of the original sample and base of the flipped sample respectively (the locations indented) to find the average cell dimensions. This ensures that any morphology change due to the release procedure is captured in the results.

Figure 2-7 shows the force-displacement curves for (a) the top surface of the unmodified 150 μm-thick sample and (b) the base surface of the sample after release. The curve shapes are typical of all the samples. The tilt of the curve at negative depth is due to the movement of the tip above the sample, an artifact of the AFM setup. The hysteresis is a signature of energy dissipation, consistent with past observed behavior [16-20]. The dip below zero force reflects adhesion between the tip and sample. The base of the films has much higher adhesion than the top surface, as described in the methods section. Due to the shallow indentations and low forces, the majority of the indentations are in the linear regime of the stress-strain response of the film, as shown in Figure 2-7c. The contact area for the stress is calculated as described in the Oliver-Pharr method, $A=\pi(2h_cR-h_c^2)$ [39]. Occasionally, for some deeper indentations at the base surface, the stress-strain curve levels off, indicating the initiation of buckling. This effect typically occurs between 8 and 20 kPa and reflects the soft nature of the base region. The top surface indentations remain in the linear regime through 80 kPa of stress.
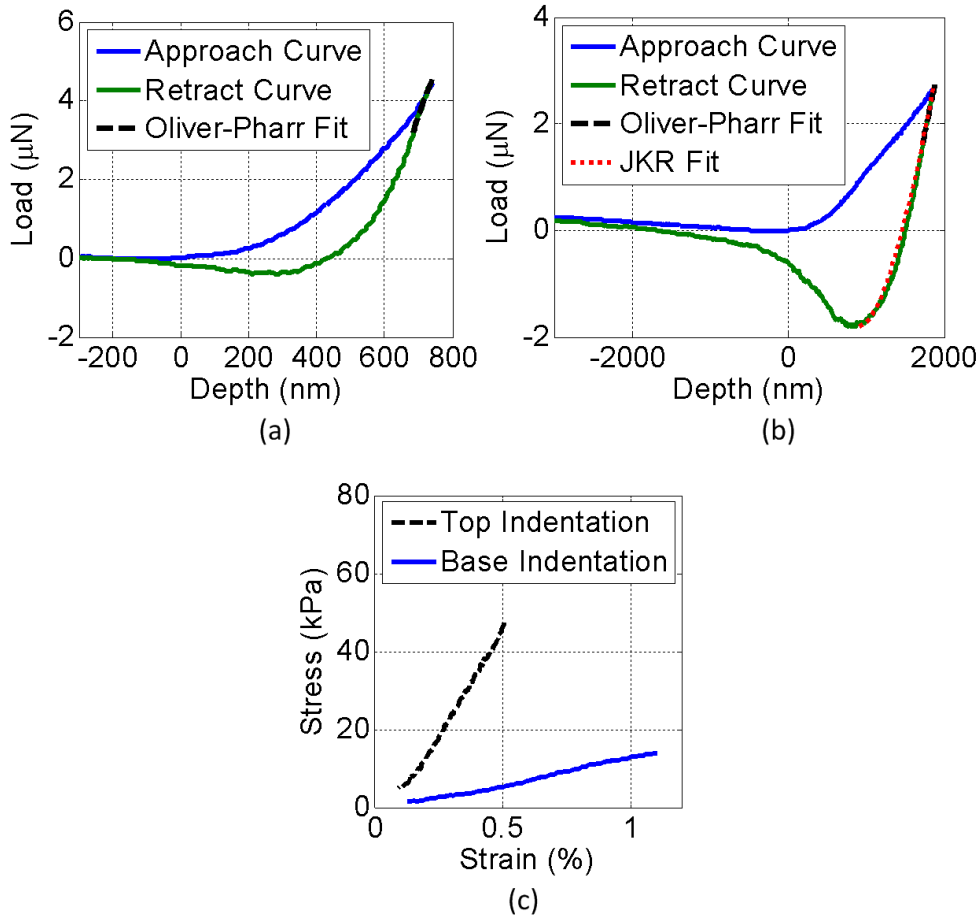
Figure 2-7: (a) Load-depth curve for the 150 μm-thick sample. "Approach Curve" corresponds to the response as the tip approaches the sample surface, and "Retract Curve" corresponds to the response of the tip moving away from the sample. The black dashed line represents the fitted slope used in the Oliver-Pharr analysis. (b) Load-depth curve for the released 150 μm-thick sample. The curve for the JKR model fit is also shown as the red dotted line. (c) Stress-strain plot of indentation from the top (dashed) and base (solid) of the 150 μm-thick sample.

Figure 2-8 shows that for the indentation measurements $E_{2,base}$ is significantly lower than $E_{2,top}$. The modulus slightly decreases with film thickness, suggesting that thicker films are more misaligned, particularly at the base of the film. This is also consistent with previous observations [24]. The values of $E_{2,base}$ in Figure 2-8 are calculated using the JKR analysis. The values of γ for the base surface range from 1.4

to 33 mJ/m^2 and are comparable to past work which showed γ between 20 and 80 mJ/m^2 for multi-walled VACNT films contacting a convex glass surface [41]. Not all the indentation curves give perfect fits to the JKR model, but the results for elastic modulus are consistent and the variations are reflected in the standard deviation.

For the range of indentation depths and the amount of variation in the data, the samples do not show a clear depth-dependent modulus. This indicates that the crust layer does not affect the response because it is negligibly thin or does not have a significantly different modulus than the top. According to the cellular model and supported by results in Won *et al.* [22], if the crust has nanotubes with mostly horizontal alignment it will have low E_2 though E_1 is high. The lack of depth-dependence also suggests that the indentations at both surfaces do not sample the properties of the well-aligned middle region.
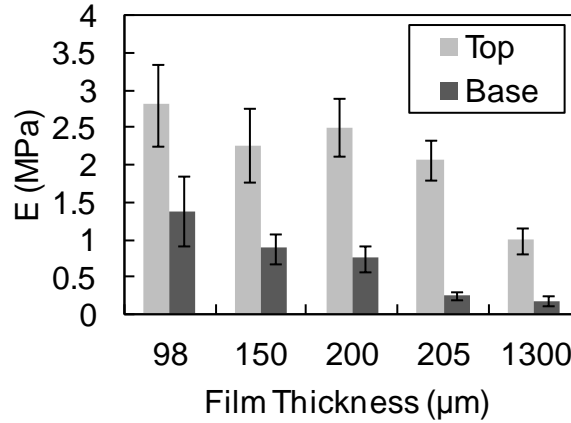
Figure 2-8: Elastic modulus measured from the top ($E_{2,top}$) and base ($E_{2,base}$) surfaces of VACNT samples of varying thicknesses. The error bars correspond to the standard deviation of the data.

To investigate the dramatic difference between $E_{2,top}$ and $E_{2,base}$, the cellular model is used to compare these values to the film morphology at the top and base. Figure 2-9 shows $E_{2,rel}$ plotted against α for each data point, after accounting for

31

differences in f. As mentioned earlier, α and f are generally equal or lower at the base region (filled data points) than the top (unfilled data points). Though the data is scattered, there is an overall trend of increasing $E_{2,rel}$ with α which suggests that the tube morphology may have a strong impact on the film mechanical properties.

In Figure 2-9 these data points are also plotted against the theoretical curve calculated from the cellular model. The overall trend of increasing modulus with alignment matches the data, though the data increases more rapidly with α than predicted. For a number of reasons, $E_{2,rel}$ of the base side may be lower than expected. The image analysis procedure may not be sufficiently effective at detecting density differences due to the depth of field of the SEM, causing errors in f if the base is actually less dense than it appears [24]. The number of defects in a CNT may increase with growth time (as reflected by the increased tortuosity) which may reduce the magnitude of E_s in the base region. There is also the possibility of unobserved weakening of the film due to the release procedure for certain samples, such as the two thickest samples. The methods to overcome these shortcomings are beyond the scope of this paper and may be resolved by measurements of more samples with a wider range of α. These results do show that a simple cellular model can explain trends in film behavior based on the morphology of the tube structure.
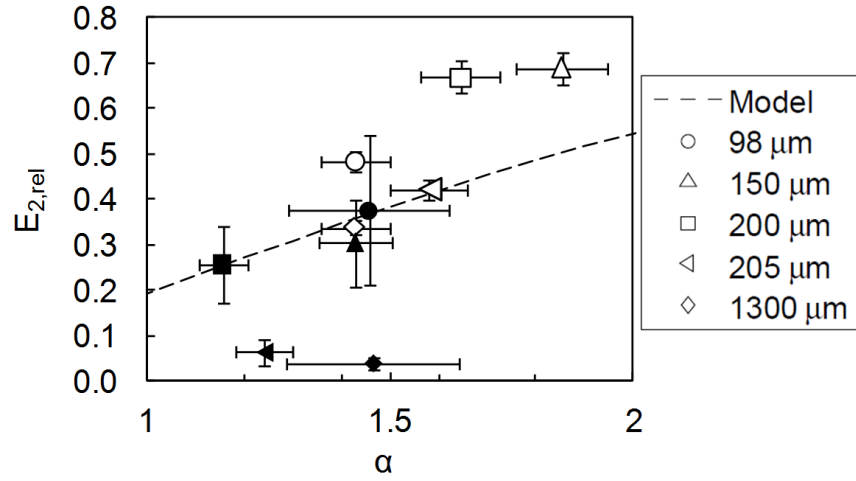
Figure 2-9: Measured modulus for all samples represented by their thicknesses. Unfilled data points represent $E_{2,rel}$ of the top surface and filled data points (corresponding to the same samples as their unfilled counterparts) represent $E_{2,rel}$ of the base surface. The cellular model is used to calculate the trendline "Model" (dashed line), with $C = 0.17$ used to fit the data to the model. Other parameters used include: $R_{out} = 4$ nm, $R_{in} = 2$ nm, and $E_s = 0.9$ TPa. α and f are determined from image data for each point. The horizontal error bars include the standard deviation of α and the vertical error bars include the error due to the standard deviations of E_2 and f for each point.

Finally, these results can be used to predict elastic modulus from image data. Figure 2-10a shows the expected local in-plane and out-of-plane moduli throughout the thickness of a VACNT film, calculated using the foam model with parameters extracted from image data and C determined from data fitting. Figure 2-10b shows the predicted modulus anisotropy ratio E_2/E_1, which is around five at the top and as low as one at the base. As expected, E_2 peaks in the middle region and is lowest at the base. E_1 and E_2 begin to converge at the base as the CNTs become more misaligned. E_1 is much lower than E_2, which agrees with past data from Deck *et al.* [17] that showed that VACNT films are nearly five times stiffer when compressed in the out-of-plane direction than the in-plane direction. This also supports past work showing low in-plane "middle" region modulus of VACNT films grown under similar conditions as

the films in this work [22]. Note that these results do not include analysis of the crust layer, which needs a different image analysis procedure. The low modulus of these films, particularly in the in-plane direction, reflects their potential suitability as compliant thermal interface materials.
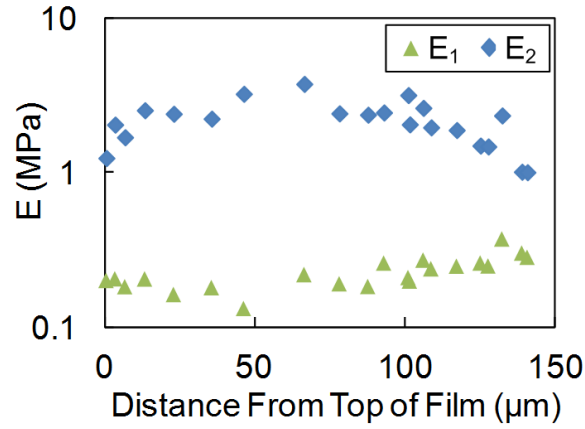
(a)
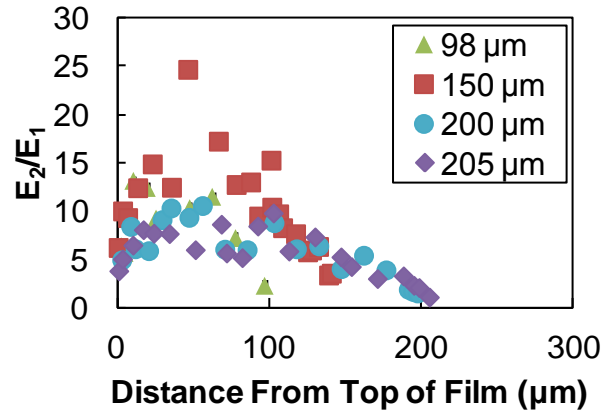
(b)

Figure 2-10: (a) Predicted E_1 and E_2 of the 150 μm-thick sample as a function of depth into the sample using the cellular model and image analysis. The vertical axis has a log scale to depict trends in E_1. (b) Predicted modulus anisotropy ratio E_2/E_1.

Figure 2-11 shows the aspect ratio of these films compared to SWCNT films grown using a different method. These films are described in Chapter 4. The SWCNT films have higher density and aspect ratio, illustrating that the structure of VACNT films depends on the growth process. The SWCNT films also exhibit misalignment towards the base.
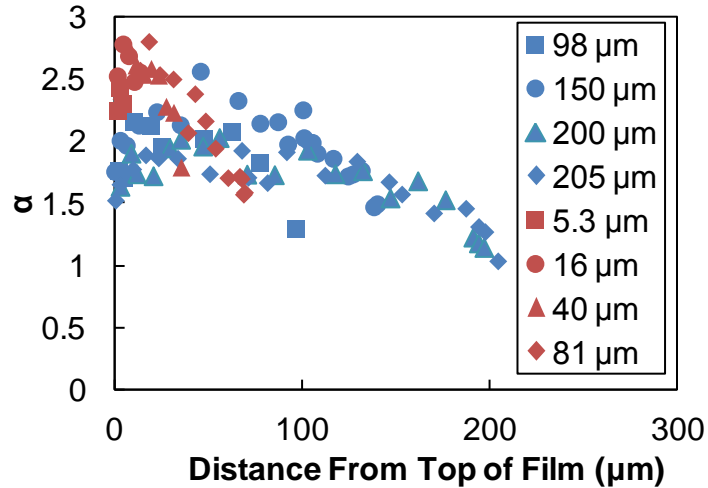
Figure 2-11: Aspect ratio of SWCNT films (red) of thickness 5.3, 16, 40, and 81 μm compared to the earlier data for these MWCNT films (blue).

2.4   Summary

We have observed the inhomogeneous structure of multiwalled VACNT films using image analysis and mechanical property measurements. Nanoindentation measurements are performed on both the top and base surfaces of VACNT films. Results show that E_2 varies significantly between the top and bottom surface, ranging from 1.0 to 2.8 MPa for the top surface and 0.2 to 1.4 MPa for the base. These data are compared to a cellular model through analysis of the tube structure using properties observed from SEM images. This technique represents a powerful new way to predict the mechanical behavior of a VACNT film, or even other types of nanostructured

35

films, using image data rather than performing mechanical measurements. Though the complex morphology of the film results in many assumptions associated with the measurement, image analysis, and cellular model, the simplicity of the study provides a broad understanding of trends in film behavior.

For further analysis, measurements can be performed on films with different structure, such as densified or unaligned films to observe the impact of greater variations in aspect ratio and density. The indentation measurement can be done with a variety of tip geometries and sizes to fully probe the effects of anisotropy and inhomogeneity of the film. A numerical model is currently being developed that will reflect a transversely anisotropic, multilayer material. This model can be used to estimate the error from the measurements if the elastic properties are estimated or measured for each direction.

Chapter 3   Assessment of VACNT Films for Thermoelectrics

3.1   Introduction

Efficient thermoelectric modules (TEMs) require low thermal resistances at the interfaces between the functional materials, the electrodes, and the heat exchangers. These interfaces must also accommodate the significant coefficient of thermal expansion (CTE) mismatch between these regions in the device. The repetitive temperature differences experienced by TEMs can exceed 1000 K, and the resulting thermal stress can degrade the quality of the interface and increase the interface thermal resistance over the module lifetime [59, 60].

Past work has demonstrated the importance of interface resistances for thermoelectric modules as well as the need for detailed thermomechanical modeling [61-64]. Pettes *et al.* [65] used one-dimensional electrothermal simulations to show that when the thermal contact conductance is decreased by a factor of ten, heat removal of a thermoelectric cooler decreases by at least 10%. LeBlanc *et al.* [66] showed that thermal interface resistances reduced the attainable electrical power output of a thermoelectric generator (TEG) in a water heater by 30% to 50%. The importance of thermomechanical studies of TEMs is emphasized in several recent works. Clin *et al.* [67] modeled stresses in TEMs due to temperature gradients across thermoelectric pellets, anisotropic CTE of the thermoelectric material, and CTE mismatch between different materials. Hori *et al.* [68] demonstrated decreasing power

output and eventual breakdown of TEMs due to deterioration of interfaces after thermal cycling. These effects necessitate a mechanically compliant and thermally conducting thermal interface material (TIM).

There has been extensive research on TIMs for microprocessors. The temperature fluctuations experienced by microprocessors are generally much less than those experienced by TEMs, allowing the use of thinner interface layers and relatively stiff materials such as metal alloys. Common interface materials include greases, solders, and polymer-based composites [1]. The thermoelectric community typically uses these commercially available TIMs.

The thermomechanical strain in thermoelectric conversion systems can be significantly larger than those in microprocessors. This calls for larger TIM thicknesses and heightens the potential benefits of a nanostructured interface solution such as a VACNT film. In a typical thermoelectric module, solder is used to make electrical contact to the pellets and thermal grease is used to improve thermal contact between the module and surrounding surfaces. This work attempts to illustrate the different property requirements of interface materials in thermoelectric systems relative to the more mature microprocessor applications.

Table 3-1 lists representative system parameters associated with TEGs and microprocessors. ΔT reflects the difference between off and on states. The TEG values are adapted from studies of waste heat recovery modules described in Vasquez *et al*. [69] The values for the BLT and microprocessor geometry are well documented in literature [1]. Figure 3-1 shows the stresses in systems using the values in Table 3-1 in Eq. 1-2 as well as the relation between thermal resistivity (R) and shear modulus (G) for each TIM. For fixed values of ΔT, α_1, α_2, L, and d, stress increases with G of the TIM. The solid lines in Figure 3-1 show that TEGs experience much higher stresses than microprocessors. The TEG pellet & metal interface has relatively low stress due to the small contact area but is still susceptible to fracture, as many thermoelectric

38

materials are brittle. The boxed areas in Figure 3-1 illustrate the tradeoff between mechanical and thermal properties in polymeric TIMs and solders. High G corresponds to solders, while low G is characteristic of polymeric TIMs such as greases and gels. A comparison of σ and R shows that though polymers may experience low stress, they typically have high R, while solders have very low R but high modulus and high stress. CNT-based TIMs approach the ideal TIM that minimizes σ, G, and R.

Table 3-1: Comparison of interfaces in representative microprocessor and thermoelectric material sets.

Interface	ΔT	CTE Mismatch $(10^{-6}/K)$	Common Joint Length (cm)	BLT (μm)
Microprocessor chip (Si) & heat spreader (Cu)	100 K	14	2	30
TEG Module (Al$_2$O$_3$) & Heat source (Cu)	600 K	8.5	7.5	100
TEG Pellet (PbTe) & Metal (Cu)	600 K	3.9	0.5	60
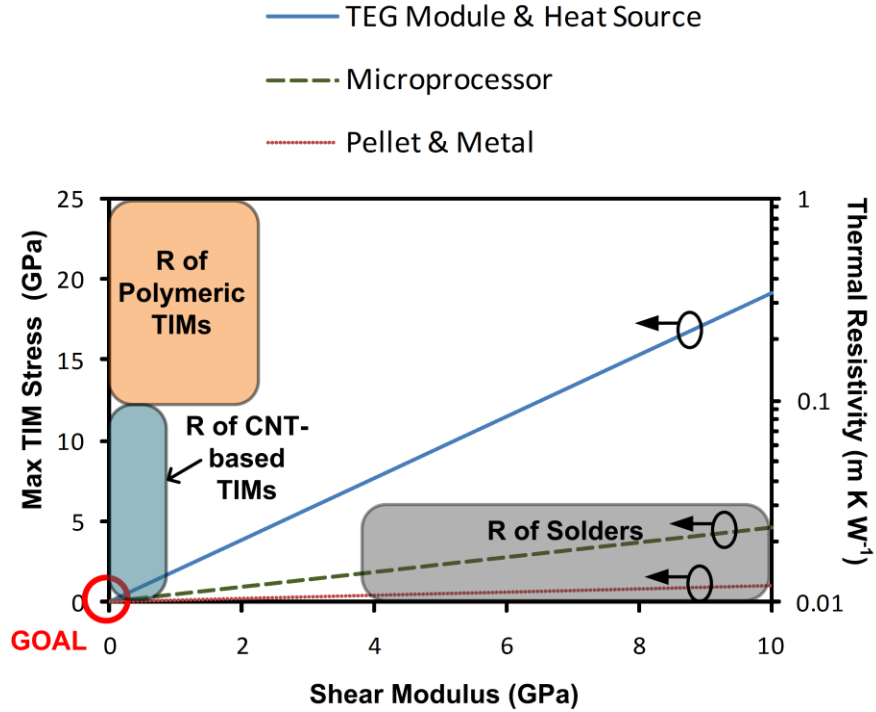
Figure 3-1: The solid lines represent maximum TIM stresses in TEG and microprocessor applications using values in Table 3-1. Polymeric TIMs range from particle-filled oils to epoxies, with *G* in the 0-2 GPa range. *G* of solders range from roughly 4 GPa (*eg.* pure In) to 10 GPa (*eg.* hard solders). The boxes represent thermal resistivity (right axis, log scale) for CNT-based TIMs, polymeric TIMs, and solders.

The solution to the thermal interface problem in thermoelectrics may be to apply VACNT TIMs around the entire module (Figure 3-2a) or between the pellet and electrical leads (Figure 3-2b). The present work studies the unique implementation of VACNT interface materials grown directly on a thermoelectric material, as in Figure 3-2b. This work characterizes the thermal properties of metal-coated multiwalled VACNT films on SiGe, a standard high-temperature thermoelectric material [70], using a nanosecond thermoreflectance technique. These results were previously published in Gao *et al*. [10].
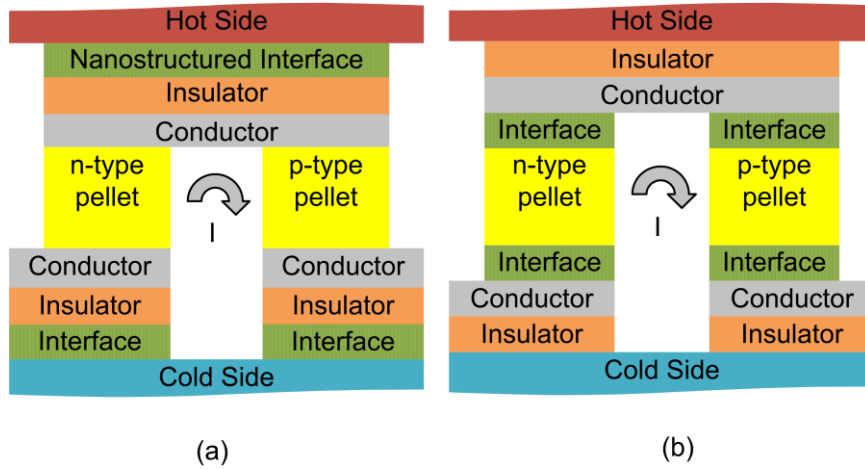
Figure 3-2: (a) A nanostructured interface material ("Interface") is used around the module. (b) a nanostructured interface material ("Interface") is used between the thermoelectric material and metal leads. Figures are based on typical TEG construction.

3.2 Experimental

3.2.1 SAMPLE PREPARATION

Among the broad variety of thermoelectric materials available, this study aims to work with one that has both technical promise and compatibility with the CNT growth process. SiGe substrates are chosen for their ability to withstand CNT growth temperatures of over 800°C. The SiGe samples are fabricated using molecular beam epitaxy on Si substrates and consist of a 2 μm buffer layer, a 1.3 μm superlattice of alternating Si and Ge, and a 0.3 μm highly-doped cap layer [71]. The samples are then prepared for the CNT growth process, which is refined for high growth yield on SiGe substrates. Sample sets are prepared both with and without an initial 100 nm-thick PECVD SiO_2 layer deposited on the SiGe substrate. Successful growth on both sample sets indicates that this SiO_2 layer is not necessary for multiwalled CNT (MWCNT) growth on SiGe. Next a 20 nm Al_2O_3 layer followed by a 10 Å thick Fe film is deposited on all samples. Annealing in oxygen produces a monolayer of Fe clusters to

act as catalysts for the CNT growth. A coupled-RF CVD plasma system is used for the MWCNT synthesis. The furnace temperature is maintained at 825°C while a mixture of C_2H_4 and Ar gases flow through the chamber for 30 minutes to produce an array of aligned nanotubes of ~1.5 μm height. Figure 3-3a shows a schematic of the samples used in these measurements, including the locations of the measured boundary resistances. A 50 nm-thick platinum film is deposited on the CNT array for thermoreflectance measurements. The scanning electron microscopy (SEM) profile of the sample in Figure 3-3b shows that the platinum layer uniformly coats the tops of the CNTs. Figure 3-3c shows that the height of the VACNT film is roughly 1.5 μm. Figure 3-3d shows the rough surface of the VACNT film. The surface topography and porous structure of the metal-coated MWCNT film can potentially pose challenges for thermoreflectance techniques. As long as voids in the metal coating are negligible and the metal is optically thick, the transmission of the laser beams is insignificant.
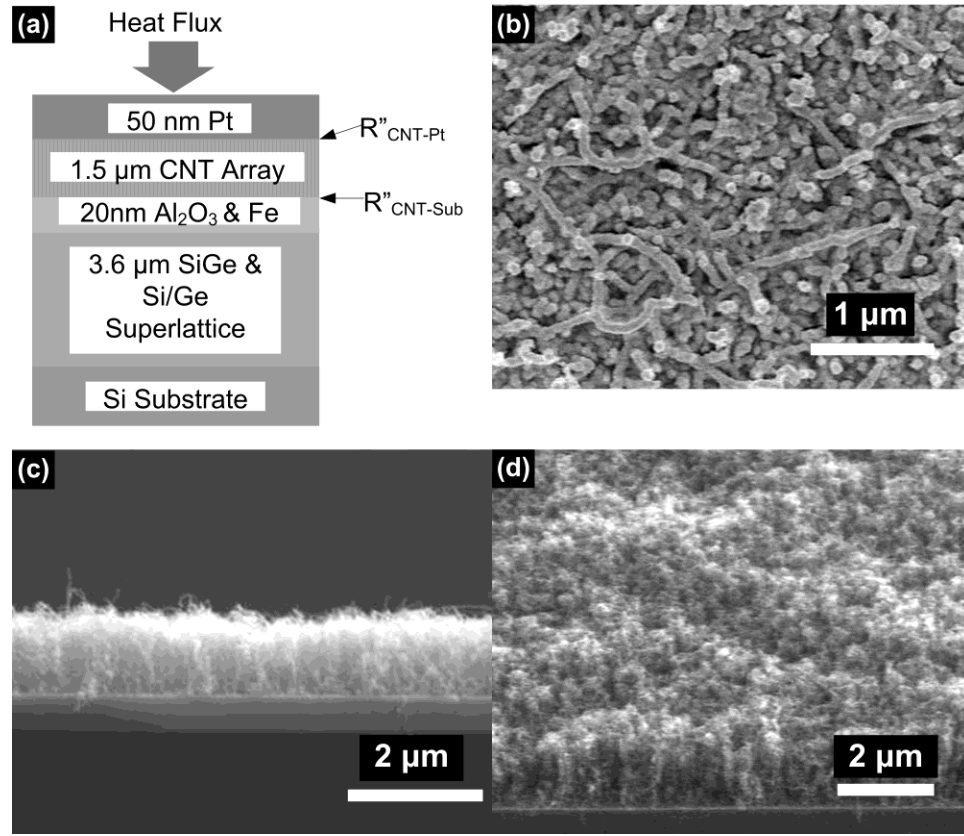
Figure 3-3: (a) Schematic of sample geometry. (b) 50 nm Pt deposited on top of CNTs, showing minimal voids. (c) cross sectional view of the VACNT film grown on SiGe / Si substrates before metallization. (d) 45° view SEM of the VACNT film.

3.2.2 MEASUREMENT TECHNIQUES

Previous work has extensively described and applied the nanosecond thermoreflectance (NSTR) technique to measuring the thermal properties of thin film materials and their interfaces [72]. Figure 3-4 shows a schematic of the thermoreflectance system used in this work. A Nd:YAG pump laser (532 nm) heat the top metal film with 6 ns pulses at a frequency of 10 Hz and spot diameter of ~3 mm, creating a transient temperature field in the multilayer stack. The reflected intensity of a continuous wave probe laser (658 nm wavelength) is proportional to the surface temperature [73], providing a dynamic measurement of the surface temperature of the

43

metal film. The probe laser is focused on the sample with a Gaussian $1/e^2$ width of ~20 μm, and a 650 MHz bandwidth photodiode measures the reflected probe beam intensity. Because the heating diameter is much larger than the maximum thermal diffusion depth during the experiments, analysis reduces to a solution of the one dimensional heat diffusion equation for a multilayer stack with surface heating that explicitly incorporates interface resistances [72, 74]. A multi-parameter least-squares fit of the transient thermal response data to the solution of the thermal model extracts the effective thermal properties of the VACNT film [72, 74].
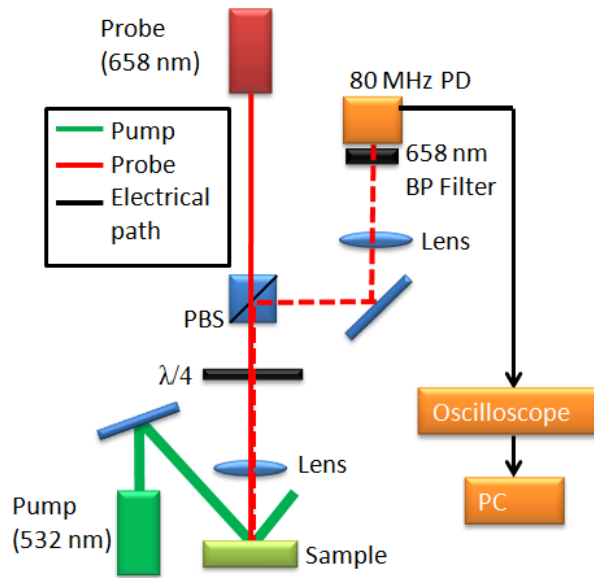
Figure 3-4: Schematic of the setup. The red dashed lines represent the probe beam reflected from the sample. "PBS" stands for polarizing beam splitter. "PD" stands for photodetector. "BP" stands for band pass. "PC" stands for personal computer.

The short timescales and unique time-dependent sensitivity of the thermal response to the thermal properties of the CNT film enable depth profiling of thermal resistances within the film and at its interfaces [72]. A comprehensive study of the impact of the variations in the thermal and physical properties (*e.g.* thickness) of each layer in the sample indicates that it is possible to extract the volumetric heat capacity

44

of the CNT film $C_{v,film}$ and the boundary resistances $R"_{CNT-Pt}$ and $R"_{CNT-Sub}$. These values can be individually resolved because each value uniquely affects the shape of the thermal response and appears separately in the analytical solution. The measurement is insensitive to the thermal conductivity of the VACNT film, k_{film} because the film is relatively thin and the boundary resistances dominate the total resistance [72, 75-77]. Nanosecond thermoreflectance measurements typically provide sensitivity to the effusivity of the sample, $e = (k_{film}C_{v,film})^{0.5}$ but in this case $C_{v,film}$ can be extracted because the response is not sensitive to k_{film}.

The experimental error and uncertainty are due to a variety of factors including signal noise and uncertainty in the material parameters that affect the extracted values. These material parameters include the local variations in the metal thickness, CNT thickness, and interface microstructure. The analytical solution is not sensitive to the thermal conductivity of the metal layer or any properties of the SiGe layer and Si substrate. The insensitivity to the CNT conductivity and SiGe properties are advantageous due to the uncertainty associated with these values.

The evolution of the thermal properties due to thermal cycling is measured by mounting the sample on a programmable INSTEC® temperature controlled stage. After applying 100 thermal cycles between 30°C to 200°C, the sample is measured using the same methods described above. The length of each cycle is roughly six minutes.

3.3   Results and Discussion

Figure 3-5 shows a representative thermal response trace for the VACNT film grown on SiGe along with the best-fit analytical solution (dashed line). The dotted line in Figure 3-5 shows that the analytical solution gives a poor fit when fitting the VACNT layer as a single resistance without also fitting $C_{v,film}$. The need to simultaneously fit

$C_{v,film}$, R''_{CNT-Pt}, and $R''_{CNT-Sub}$ proves that the measurement sensitive to the individual boundary resistances rather than a lumped total resistance of the array.
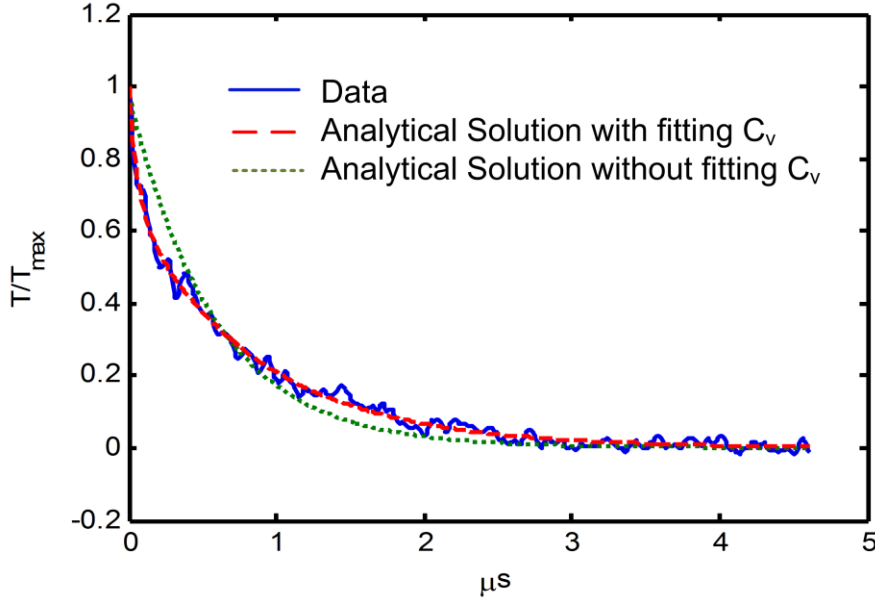
Figure 3-5: Thermal response trace data (solid) and best-fit analytical solution (dashed) for the VACNT film grown on SiGe measured using nanosecond thermoreflectance. T/T_{max} is normalized surface temperature. The dotted line shows a poor fit when the CNT layer is fitted as a lumped total resistance.

Table 3-2 shows the fitted parameters before thermal cycling averaged over multiple measurements at three locations on the sample, as well as the uncertainty associated with each value. The effective fill fraction f of the VACNT film can be estimated by comparing $C_{v,film}$ to the volumetric heat capacity of an individual MWCNT, $C_{v,ind}$ [72]. The heat capacity c_p of MWCNTs is taken to be that of graphite, 710 J kg^{-1} K^{-1} [78] and the density ρ is 1.34×10^3 kg m^{-3} [79] giving $C_{v,ind}$ of roughly 1 MJ m^{-3} K^{-1}. f is given by $f = C_{v,film}/C_{v,ind}$.

The measured value of $C_{v,film}$ gives $f = 0.9\%$. MWCNT arrays typically have 0.5 - 10% volume fraction [77, 80]. The uncertainty in R''_{CNT-Pt} and $R''_{CNT-Sub}$ are due

mainly to variations across the sample and uncertainty in the Pt thickness. The uncertainty in $C_{v,film}$ is due largely to the uncertainty in CNT height, which is estimated to be between 1 μm and 3 μm based on the SEM images.

Table 3-2: Averaged best-fit values for the extracted properties of the CNT film grown on SiGe/Si substrate.

Parameter	Average Result	Uncertainty (%)
$R''_{CNT\text{-}Pt}$	1.4 m^2 K MW^{-1}	30
$R''_{CNT\text{-}Sub}$	4.3 m^2 K MW^{-1}	40
$C_{v,\,eff}$	87 kJ m^{-3} K^{-1}	50

$R''_{CNT\text{-}Pt}$ and $R''_{CNT\text{-}Sub}$ match with previously reported boundary resistance values, which are typically between 1 to 100 m^2 K MW^{-1} for MWCNT arrays [77, 81]. Assuming a lower bound of k_{eff} of 1 W m^{-1} K^{-1} gives a bulk film resistance of 1.5 m^2 K MW^{-1}. This with the best fit values for $R''_{CNT\text{-}Pt}$ and $R''_{CNT\text{-}Sub}$ gives a total film resistance R''_{tot} of 7.2 m^2 K MW^{-1}. This is analogous to a 21.6 μm layer of thermal grease at $k = 3$ W m^{-1} K^{-1} without boundary resistances. In practical applications of the VACNT film, the boundary resistances may be reduced with the use of a eutectic-based binder material that maintains good thermal contact with more tubes [77].

Thermal cycling results of the same sample are shown in Figure 3-6. There seems to be little effect on thermal resistance after 10 cycles. There is roughly a 15% increase in $R''_{CNT\text{-}Sub}$ after 100 cycles, but this difference is still within the error range and not necessarily an indication of sample damage. Further study is needed to confirm the effects of thermal cycling.
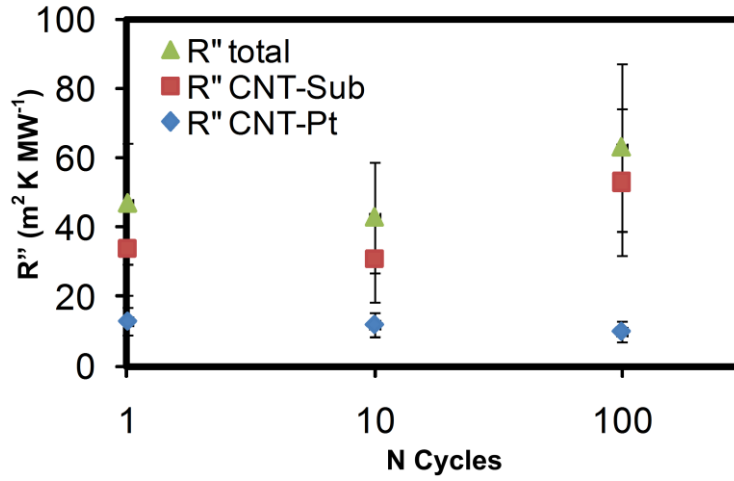
Figure 3-6: Effect of thermal cycling from 30°C to 200°C on VACNT film boundary resistances. N is the number of cycles.

3.4 Summary

This work addresses the different interface requirements between thermoelectric and microprocessor applications and studies the relevance of using VACNT thermal interface materials for thermoelectric systems. We explain the benefits of using a nanostructured TIM, demonstrate VACNT growth on thermoelectric material, and measure the thermal boundary resistances and heat capacity associated with the VACNT film. The boundary resistances can be reduced in future studies with application of adhesion layers around the VACNT film and by improving the VACNT growth to obtain thicker films. Thermal cycling does not have a significantly detrimental effect on the VACNT array, though further studies are necessary, as well as comprehensive imaging of the sample before and after cycling. Future work also includes studying nanostructured interfaces in actual thermoelectric devices.

Chapter 4   Thermal Characterization of Single-Wall VACNT Films

4.1   Introduction

Thermal interface materials (TIMs) are critical for a variety of applications including microprocessors and thermoelectric power generators [1, 10, 82]. The temperature drop across these interface materials is a key factor influencing the reliability of computers and the efficiency of thermoelectric generators. Though compliant materials such as thermal greases mitigate reliability concerns resulting from mismatches in the coefficient of thermal expansion (CTE) at interfaces, they do not conduct heat as well as a solder joint. Recently there has been interest in TIMs based on vertically aligned carbon nanotube (VACNT) films. A VACNT film makes use of the high axial thermal conductivity and flexibility of individual carbon nanotubes (CNTs) and avoids drawbacks of polymer-based greases such as pump-out, drying, and degradation at high temperatures [1, 82]. VACNT films can currently be grown to millimeters in height and on a variety of substrate materials, including metals [83, 84]. They are promising for applications with large CTE mismatch or substantial gaps between the contacting surfaces.

Given the wide range of past data on VACNT thermal properties, there is a need to better understand and improve the performance of these films. The thermal conductivity, heat capacity, and boundary resistances of the films are all important properties and past measurements have only determined one or two properties at a time. VACNT films also have a complex morphology that can affect the thermal and

mechanical behavior of the film. The thermal properties are rarely linked to analysis of the film morphology.

Past measurement and simulation of the thermal conductivity of an individual nanotube, k_{ind}, ranges from around $34 - 10,000$ W m^{-1} K^{-1} [4, 85, 86], with most values around 3,000 W m^{-1} K^{-1} [4-7]. Most modeling of nanotubes is performed on single-wall CNTs (SWCNTs) due to the complexity of multiwalled CNTs (MWCNTs). Though individual MWCNT have been measured to have k_{ind} as high as 3,000 W m^{-1} K^{-1} [6, 7], Pettes *et al.* measured a significantly lower k_{ind} in their MWCNT compared to their SWCNT, possibly due to increased defects in the MWCNT [87].

Previous measurements of the effective thermal conductivity of VACNT films, k_{film}, have nearly all been performed on MWCNT films. This is in part due to the difficulty of growing vertically-aligned SWCNT films, though SWCNT films generally have higher CNT quality [88, 89]. Past work measuring MWCNT films report k_{film} ranging from 0.5 W m^{-1} K^{-1} to 267 W m^{-1} K^{-1} [12, 76, 78, 79, 81, 90-95]. Most of these values of k_{film} are much lower than predictions based on scaling the ideal $k_{ind} = 3000$ W m^{-1} K^{-1} by f, the nominal volume fraction of CNTs in the film. A review of past measurements of k_{film} scaled by f is provided in Gao *et al.* [10]. The specific reasons for the relatively low and scattered values of k_{film} remain poorly understood – the mechanisms may be due to the lower quality of CNTs in a film compared to the high-quality tubes used for individual tube measurements, effects from tube-tube interaction, or poor engagement between the film and surrounding materials. The quality of the contact between the film and surrounding surfaces also affects boundary resistances, which can be a significant contribution to the total thermal resistance of the VACNT layer [12, 95, 96].

There have been few measurements of both k_{film} and film heat capacity for a given film. The volumetric heat capacity of the film, $C_{v,film}$ is sometimes estimated using f and then used to extract thermal conductivity from thermal diffusivity (α) or effusivity (e) measurements [78, 91, 94]. $C_{v,film}$ is related to f through the density and heat capacity of an individual nanotube. The value of f is typically estimated from

50

image analysis or mass measurements. Previous observations of the nanotube structure show that the CNT density and alignment in a VACNT film can vary throughout the film thickness [24, 31, 97], which may result in errors in density calculated from image estimates. Furthermore, if there are nanotubes present that do not participate in thermal conduction, the heat capacity will be overestimated [98]. Thus k_{film} and $C_{v,film}$ should be measured separately for each film.

The present work represents the first study on the thermal properties of a set of seven high quality single-wall VACNT film samples grown under identical conditions over a range of thicknesses. A frequency domain thermoreflectance technique is used to extract a set of thermal properties including k_{film}, $C_{v,film}$, and boundary resistances. The surface roughness of the metalized films is characterized using an atomic force microscope (AFM). The film morphology is quantified using image analysis and provides insight into its thermal response. This also serves as a method to quantify the difference between samples, which may help explain the wide variation in past measured thermal properties.

4.2   Sample Preparation

Vertically aligned SWCNT films are grown by alcohol catalytic chemical vapor deposition at 800°C with ethanol as the carbon source. Details of the synthesis and growth procedure have been previously reported in literature [89, 97, 99, 100]. The Si substrates are fabricated by means of growth of a 50 nm SiO_2 layer, followed by evaporation of catalyst films of 10 nm Al and 0.2 nm Co. This growth procedure produces SWCNT with an average diameter of 2 nm. The number density of nanotubes is around 10^{15} m^{-2} [101]. The nanotubes often form bundles, typically composed of 5 - 6 tubes [101].

Growth times are varied to yield seven SWCNT film thicknesses of 5.3, 6.3, 16, 40, 42, 45, and 81 μm. The mass densities of the SWCNT films are determined using their measured mass, thicknesses, and areas. The mass of the sample before and after the SWCNT growth is measured using a microbalance (SE2 Ultra Micro

51

Balance, Sartorius) and confirmed by removing the SWCNT film and re-weighing the substrate. The thickness of the SWCNT films is obtained from cross-sectional SEM images. The measured mass density of 94 – 102 kg m^{-3} translates to ~7% volume density, assuming an individual SWCNT density of 1.5 g cm^{-3} based on the density of graphite (2.23 g cm^{-3}), graphite interlayer spacing (0.34 nm), and radius of the SWCNT (1 nm).

For the thermal measurements, a 100 nm-thick Ti layer is evaporated on top of the SWCNT array as an adhesion layer, followed by a 100 nm-thick Ag film for high optical reflectance. The sample structure is shown in Figure 4-1a, with a cross-sectional scanning electron microscope (SEM) view of the film shown in Figure 4-1b. The SEM images of the sample in Figure 4-1c and d show that the metal forms a discrete layer over the nanotubes, with pore diameters <100 nm. The rough surface of the metal-coated VACNT film often poses a challenge for thermoreflectance measurements. Past techniques for overcoming this include heating the film through transparent substrates coated with metal layers which are then bonded to VACNT films, but these require more specialized sample preparation [77, 81]. Because of the rough nature of the film, there is some uncertainty regarding the heat capacity and thickness of the film - these are discussed later.
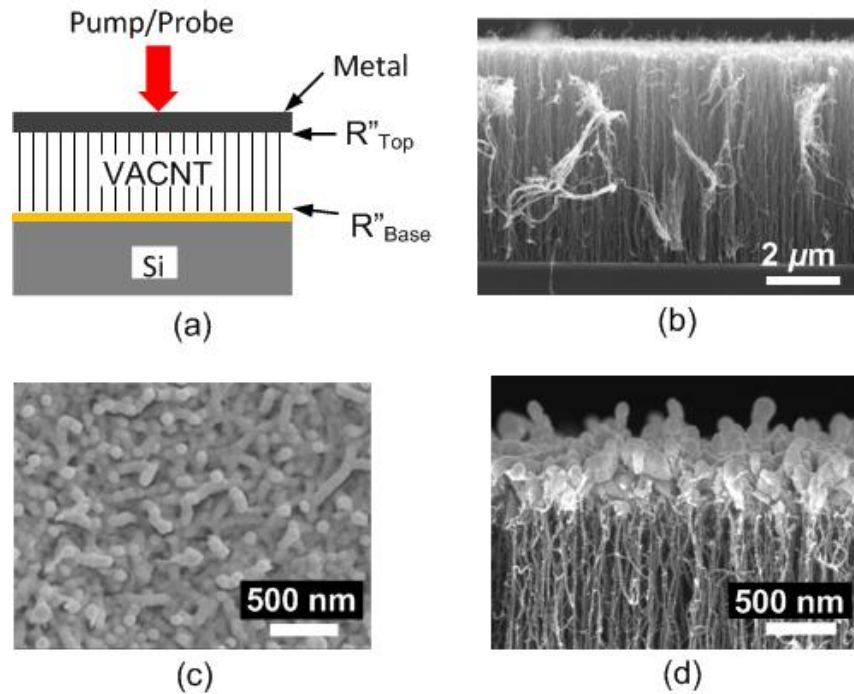
Figure 4-1: (a) Schematic of the sample structure for thermoreflectance measurements. The top and bottom boundary resistances are indicated by R''_{top} and R''_{base} respectively. (b) Cross-section of a VACNT film on Si. (c) Top-down SEM image of the metalized surface of a SWCNT film. (d) SEM image of a cross-section of a SWCNT sample, showing the metal layer on top of the vertically-aligned nanotubes.

For image analysis, the VACNT samples are first split by cleaving the Si substrate to gain visual access to the CNTs away from the sample edges. The cleaved edge is sputter coated with ~4 nm Au to enhance SEM image contrast. Images of the film are taken using a FEI XL30 Sirion SEM from the top to the base of the film. The image analysis and procedure to extract alignment and volume fraction are described in Chapter 2.

The surface roughness of the metalized VACNT films is examined using a Topometrix Explorer scanning probe microscope in contact mode. The VACNT films without a metal layer did not provide clear images due to the soft and porous film surface. The AFM cantilevers used have silicon nitride tips with 20 nm radius. At least three images with scan size 10 μm square or 20 μm square are taken of each sample.

Images are leveled and horizontal strokes are corrected using data analysis software (Gwyddion 2.22) before the root mean square (RMS) roughness is calculated. Figure 4-2 shows the results of AFM surface topography measurements. There does not appear to be a strong trend with film thickness.
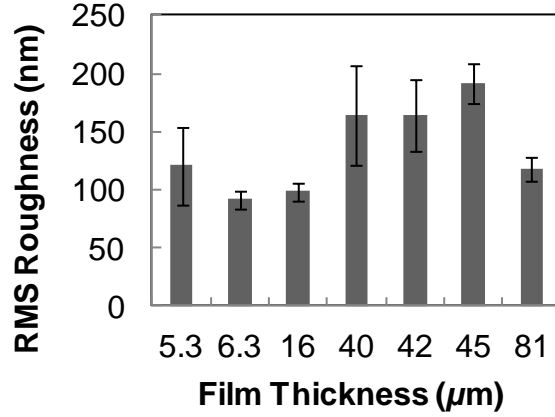
Figure 4-2: RMS surface roughness of metallized SWCNT films. The error bars are based on the standard deviation between images.

4.3 Thermal Measurements

4.3.1 EXPERIMENTAL APPARATUS

The films are measured using two optical non-contact methods: a nanosecond thermoreflectance (NSTR) technique and a frequency domain thermoreflectance (FDTR) technique. The NSTR experimental setup and theory has been described in detail in previous work [96, 102]. The FDTR method has also been well documented in past literature [74, 103, 104]. This work describes this particular setup for the first time. This FDTR setup is integrated with the NSTR rig, where the sample is located at the same position and the probe laser and photodetector are shared. The FDTR setup provides sensitivity to individual material properties, as explained in the following section, and the NSTR technique is only used to confirm the FDTR results for these measurements.

Figure 4-3 shows the FDTR setup, in which the intensity of a heating laser, or "pump" (Nd:YAG, 1064 nm) is modulated by an electro-optic modulator (EOM) (Conoptics, Inc. Model 360) that is controlled by a high voltage analog driver (Conoptics, Inc. Model 25A, DC to 30 MHz). A function generator controls the modulation frequency of the EOM. An optical isolator is placed before the EOM to prevent back reflections into the laser cavity that cause instabilities in the heating beam.

The pump heats the metalized surface of the VACNT sample with a sinusoidal heat flux. A probe beam (658 nm wavelength) is reflected off the surface and the amplitude of the reflected beam is detected by an 80 MHz balanced photodiode (New Focus™, Model 1807). The reflectivity of the metal film is proportional to its temperature, so the reflected intensity of the probe provides the temporal dependence of the sample's surface temperature. The photodiode is operated in balanced mode to increase the signal to noise ratio and includes 658 nm band-pass filters on both detectors. The photodiode voltage is sent to a lock-in amplifier that can operate from DC to 100 kHz (Stanford Research Systems, Inc. Model SR830). Lock-in amplifiers can detect the amplitude and phase shift of signals with poor signal-to-noise ratios by locking in to the fundamental frequency of the signal and rejecting all other frequencies. The function generator used to control the EOM also sets the reference frequency and phase of the lock-in.

The amplitude and phase shift of the pump beam is determined in the same manner by detecting the pump beam reflected off the sample using the same optical path and components (photodetector, cables, etc). This is used to find the amplitude and phase shift due to the sample of interest by accounting for phase and amplitude shift of the setup itself. To do this the probe amplitude is divided by the pump amplitude, after both are normalized, and the pump phase shift is subtracted from the measured probe phase shift.

The amplitude shift and phase delay of the reflected probe beam relative to the heating beam depends on the thermal properties of the sample and the frequency of

heating. The solution to the three-dimensional, radially-symmetric heat diffusion equation for a multilayer stack [74] is fit to the phase shift and normalized magnitude data using a multi-parameter, least-squares fitting algorithm. The sample structure consists of a semi-infinite air layer, metal layers, VACNT film layer, and semi-infinite Si substrate layer with boundary resistances between each layer. This allows extraction of the effective thermal properties of the VACNT film and its interfaces.

Both the pump and probe beams are focused onto the sample using a 10× objective lens. The radii of the heating and probe spot affect the thermal response and can be tuned by adjusting the divergence of the beams. For these measurements a $1/e^2$ heating spot radius (r_{pump}) of 183 μm is chosen. The large heating diameter allows the spot size to be directly measured using a CCD beam profiler (Thorlabs, Inc. BC106-VIS) and reduces the temperature rise of the region. It also reduces sensitivity to the film anisotropy, which is assigned a value based on past literature. The probe radius (r_{probe}) is calculated to be 8 μm at the focus by fitting a set of beam widths, measured by the beam profiler, to a Gaussian beam profile. The thermal response has low sensitivity to r_{probe}. The beam profiler is also used to ensure that the beams are coaxial. The maximum temperature rise of the sample is given by $\Delta T_{avg} = Q_{avg} /(2\sqrt{\pi} r_{pump} k)$ where Q_{avg} is the average laser power and k is the thermal conductivity of the substrate [74, 104]. The average absorbed heating power is estimated to be 20 mW using a power meter and the reflectivity of Ag. For the worst case scenario of a semi-infinite, low conductivity CNT film with $k = 2$ W m^{-1} K^{-1}, the temperature rise is around 15 K.
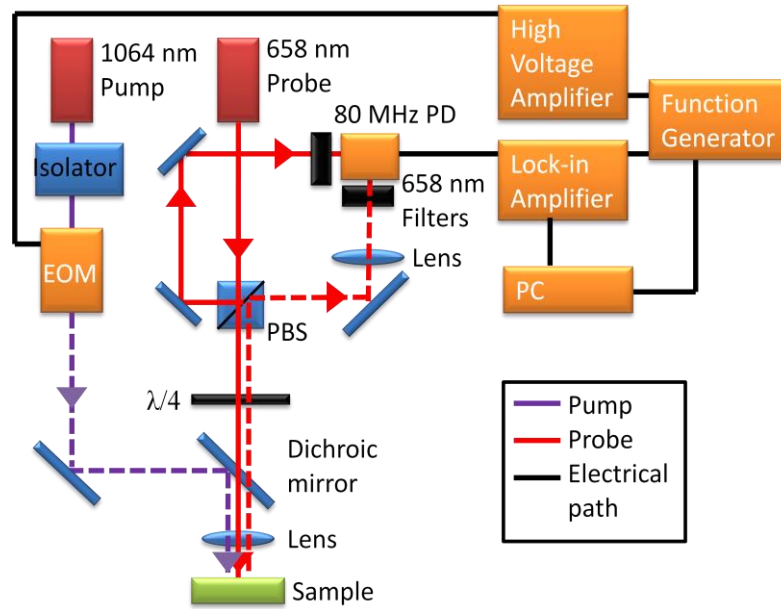
Figure 4-3: Schematic of the FDTR setup. A PC controls the function generator and captures data from the lock-in amplifier, allowing sweeps over various frequency ranges at a customizable data rates and sensitivities. The photodetector is a balanced detector; the photodiode depicted on the lower edge detects the modulated probe beam and the detector on the left edge captures the unmodulated probe beam. The intensity of the two beams is adjusted using filters and wave plates.

4.3.2 DATA ANALYSIS AND UNCERTAINTY

Thermoreflectance measurements are particularly challenging for CNT films because the thermal response of these samples is independently sensitive to as many as four thermal properties, depending on their relative magnitudes and the thermal diffusion depth. These include $C_{v,film}$, k_{film}, R''_{top}, and R''_{base}. The thickness of the CNT film and the properties of the metal layer and substrate are set as known values. Figure 4-4 shows examples of imperfections in a VACNT film that affect the unknown parameters. Figure 4-4a shows how incomplete CNT-metal contact can create thermally isolated CNTs due to high CNT-CNT thermal resistance. These isolated nanotubes (in blue) would not contribute to thermal conduction and heat capacity, but

they would be included in mass measurements and image estimates of f. Figure 4-4b indicates that CNT-CNT contact may reduce k_{ind} by affecting phonon modes in a CNT. Figure 4-4c shows how defects may also reduce k_{ind} by acting as scattering sites for phonons and can create kinks in the nanotube structure. Figure 4-4d shows that reduced density at the base of the film may affect the calculated f of the film, though if the nanotubes contact the top metal layer they will still contribute to heat capacity in a thermoreflectance measurement. This also illustrates decreasing nanotube alignment towards the base, which may indicate defects and increased tube-tube contact. The detachment of tubes may also manifest as a high boundary resistance.

The values of f and k_{ind} for CNT films are unknown but can be related to the previous four unknown parameters as follows. For the analysis, f is defined as the volume of tubes that contribute to thermal conduction within the film, $k_{film} = f \times k_{ind}$. An equal number of nanotubes should contribute to heat capacity and thermal conductivity, giving the additional condition $C_{v,film} = f \times C_{v,ind}$, where $C_{v,ind}$ is the volumetric heat capacity of an individual SWCNT. $C_{v,ind}$ is assumed to be 1 MJ m^{-3} K^{-1}, assuming the specific heat of a SWCNT is that of graphite, 710 J kg^{-1} K^{-1}, and the density of a SWCNT is 1.5 g cm^{-3}.

Though it is possible to simultaneously fit four unknown parameters, during data fitting there are often multiple solutions that fit a single thermal trace. In many cases, a thermoreflectance measurement may only be sensitive to α or e. This is the case for the NSTR technique, which gives sensitivity to e. The advantage of the FDTR technique is that it provides sensitivity to k and C_v separately due to radial heat spreading [104, 105]. Sensitivity is defined as

$$S = \frac{\% \text{ change in Y}}{\% \text{ change in X}} = \lim_{\Delta Y, \Delta X \to 0} \frac{\Delta Y / Y_o}{\Delta X / X_o}$$

(4-1)
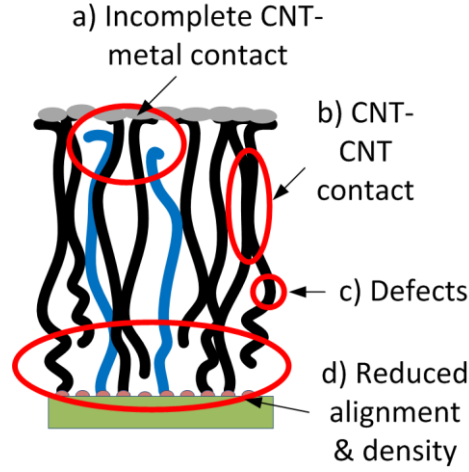
Figure 4-4: Diagram of a VACNT film coated with a metal layer (gray) grown from catalysts (orange) on a substrate (green). Various imperfections in a VACNT film, which govern the properties extracted in the present work, are illustrated.

Sensitivity is generally dictated by the thermal diffusion depth (L_p) into the sample, the degree of radial heat spreading, and the relative contribution of a parameter to the overall thermal response. Thermal diffusion depth is given by $L_p = \sqrt{2\alpha/\omega}$ where ω is the angular frequency of the heating. These effects are illustrated by the following examples. At a frequency of 1 kHz and α of 55 mm^2 s^{-1}, L_p = 132 μm, whereas at a frequency of 100 kHz, L_p = 13 μm. If L_p is much lower than the thickness of the film, the results will not be sensitive to R''_{base}. If the ratio of r_{pump} to L_p is high, the thermal diffusion through the sample will become one-dimensional and the thermal response will only give sensitivity to e. For the VACNT films less than 40 μm thick, the thermal response is not sensitive to k_{film} because the contribution of the film resistance to the overall thermal response is small. Similarly, the sensitivity to R''_{top} decreases when R''_{top} is small.

Figure 4-5 shows the sensitivity of amplitude and phase to various parameters, illustrating how the sensitivity to each parameter is unique over the frequency range. The response exhibits unique sensitivity to k_{film} and $C_{v,film}$ and low sensitivity to R''_{top}.

59

For example, at around 16 kHz the phase response has zero sensitivity to k_{film} but has some sensitivity to $C_{v,film}$. The magnitude generally exhibits low sensitivity to k_{film} but not $C_{v,film}$. Near 100 kHz, the phase response exhibits sensitivity to e with no distinction between k_{film} and $C_{v,film}$. This is because as frequency increases, the thermal diffusion depth decreases, resulting in one-dimensional heat flow. The sensitivity to R''_{base} is also unique but is not shown for clarity.
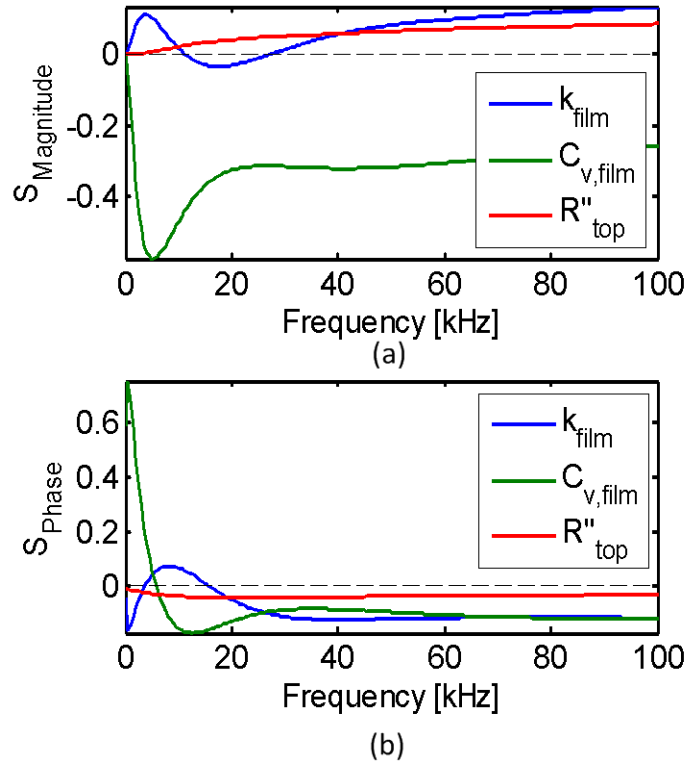
Figure 4-5: The theoretical sensitivity to changes in k_{film}, $C_{v,film}$, and R''_{top} for (a) the magnitude response and (b) phase response based on measured values for the 45 μm-thick sample. The dashed line indicates zero sensitivity.

Uncertainties due to local variations in the metal thickness, CNT thickness, and signal noise contribute to the scatter in the data. These errors are captured by taking multiple measurements per sample; each sample is measured at three different

locations on the sample with at least two data sets per spot. This gives the standard deviation of the data at each frequency.

There is a range of possible best-fit solutions for each data set that fall within the scatter of the data. A single four-parameter fit would only represent one possible solution in the solution space. To interrogate the full range of values that fit the data, the following procedure is done for each sample over each of the four variables. The value of one variable is fixed (*e.g.* k_{film}) while data fitting is performed on the other three variables (*e.g.* $R"_{top}$, $C_{v,film}$, $R"_{base}$). This is repeated to find the minimum and maximum values of the fixed variable that give good fits to data (*e.g.* k_{film} = 2 - 4 W m^{-1} K^{-1}). For example, if k_{film} for the thickest sample is assumed to be 50 W m^{-1} K^{-1}, there is no combination of variables that give a good fit to data, thus k_{film} cannot be that value.

Bounds on each parameter, shown in Table 4-1, are used during data fitting to limit the solution space. The lower bound of the boundary resistances represents the typical contact resistance between two smooth well-contacted surfaces and is based on values from past modeling of CNT-substrate and graphene-metal contact resistance [98]. The upper bound is an order of magnitude higher than the highest measured boundary resistance for VACNT films. The range of k_{film} is based on the range of past measured data on VACNT films. The upper limit of f is based on the highest expected density of these VACNT films and is higher than the measured mass density of 7%. Anisotropy ranges between perfectly anisotropic (zero) to perfectly isotropic (one). The expected value of 0.01 is based on previous measurements of anisotropy which range from 0.014 to 0.042 [81, 91, 106] and the observation that these nanotubes are well aligned. The other expected values in Table 4-1 represent the initial guesses used during data fitting. The results are independent of these values.

Table 4-1. Bounds for each unknown parameter and expected values.

Parameter	Lower Bound	Upper Bound	Expected value
R''_{top} (m^2 K MW^{-1})	0.001	1000	1
k_{film} (W m^{-1} K^{-1})	0.5	300	5
f (%)	1	10	7
R''_{Base} (m^2 K MW^{-1})	0.001	1000	1
Anisotropy	0	1	0.01

There are also errors due to the uncertainty in known parameters such as the thicknesses of each layer, known thermal properties, and spot sizes. This is calculated using standard error propagation techniques given by

$$\Delta Z_i = \sqrt{\sum_j \left(\frac{\partial Z_i}{\partial j} \Delta j \right)^2} \qquad (4\text{-}2)$$

Here Z_i are the extracted parameters k_{film}, $C_{v,film}$, R''_{top}, and R''_{base} and j are the modeling parameters. ΔZ_i represents the error of each parameter. The thermal conductivity of the metal layers and the properties of the Si substrate are assumed to have low uncertainty and contribute negligibly to the total error.

Table 4-2 shows that the errors due to these parameters are much lower than the error due to the scatter in the data, except for the error in k_{film} due to uncertainty in the thickness and heat capacity of the metal.

Table 4-2: Example uncertainty analysis for the 45 μm-thick SWCNT film. L_{metal} represents the thickness of the metal layers and L_{CNT} represents the thickness of the SWCNT film. ΔZ_i are given in the last four columns. The uncertainties in the metal layer dominate the total uncertainty for each variable.

Parameter	Nominal value	Uncertainty	Δk_{film} (W m^{-1} K^{-1})	Δf	$\Delta R"_{top}$ (m^2 K GW^{-1})	$\Delta R"_{base}$ (m^2 K GW^{-1})
L_{metal}	200 nm	10 nm	0.12	0.01	11	338
$C_{v,metal}$	2.47 MJ m^{-3} K^{-1}	10%	0.12	0.01	13	346
Anisotropy	0.01	0.01	0.02	0.00	6	47
L_{CNT}	45 μm	1 μm	0.08	0.00	0	2
r_{pump}	183 μm	5 μm	0.07	0.00	34	31
r_{probe}	8.5 μm	2 μm	0.00	0.00	1	13
Total uncertainty	--	--	0.20	0.01	38	488

4.4 Results and Discussion

Figure 4-6 shows an example of the best fit magnitude and phase response to data for the 45 μm sample. The best fit values that fall within the error range are reported in the results.
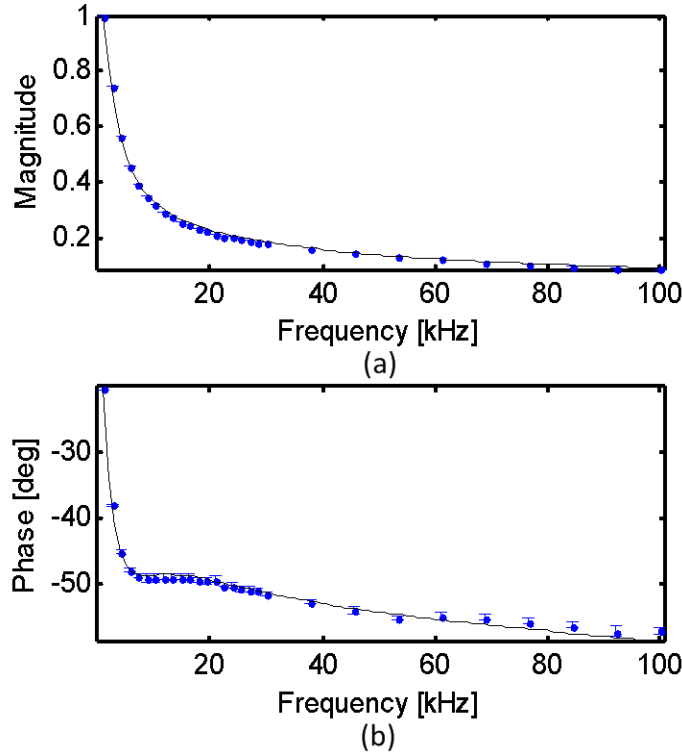
Figure 4-6: FDTR data and best fit solution for the (a) magnitude response and (b) phase response for the 45 μm sample. The data points include error bars representing the standard deviation of the data. A higher number of data points are taken at frequencies below 30 kHz because the sensitivities are stronger and there is a higher rate of change in that region.

The results from the thermoreflectance measurements of the SWCNT films are shown in Figure 4-7. The error bars encompass the full range of possible solutions. The extracted film properties all fall within those reported in past literature. As mentioned earlier, there is low sensitivity to the properties of the VACNT film itself as the film thickness decreases below 40 μm. k_{film} is not reported for those films and the error bars for f are larger.

Figure 4-7a shows that the average values of k_{film} range between 2.1 and 3.5 W m^{-1} K^{-1}. In Figure 4-7a, the results from the FDTR measurement are compared against

NSTR measurements to check for consistency. The NSTR data is fit using a set value of f from the FDTR results and match well with the FDTR results. Figure 4-7b shows the best fit values for f. $C_{v,film}$ ranges from 5.5 to 9.3 J cm^{-3} K^{-1} and the values of α range from 37 to 56 mm^2 s^{-1}. This is comparable to past data of α which range from 42 to 90 mm^2 s^{-1} [81, 91, 106]. The large uncertainty in f for some samples in makes it difficult to discern any trends with thickness.
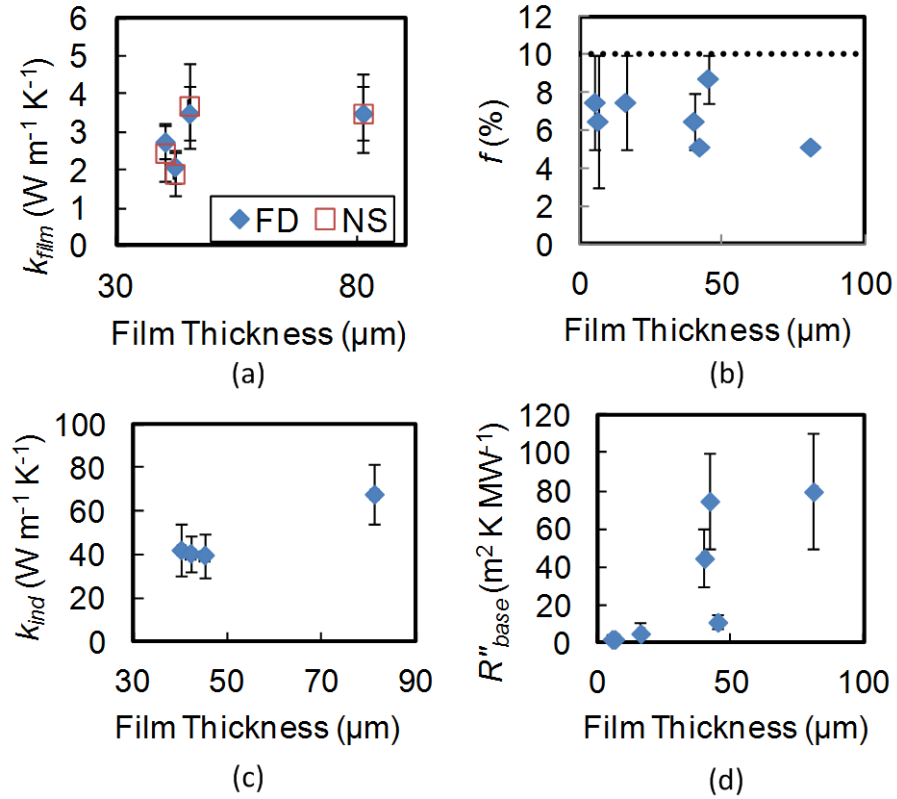
Figure 4-7. (a) k_{film} of each sample represented by the film thickness. "FD" represents data taken using FDTR while "NS" represents data taken using NSTR. (b) f of each sample with $f = 10\%$ as the upper bound (dashed line). (c) k_{ind} calculated from data in (a) and (b). (d) $R"_{base}$ of the SWCNT films.

Figure 4-7c shows k_{ind} calculated from the data in Figure 4-7a and b using the relationship $k_{film} = f \times k_{ind}$ given earlier. The results are much lower than the ideal values of $k_{ind} = 3000$ W m^{-1} K^{-1} though they match well with past values of k_{ind} extracted from measurements of VACNT films [81, 90, 91, 93, 95, 106]. There may

be low k_{ind} from an increased probability of defects, vacancies, and impurities with tube length [91, 107-109]. Defects can develop during CNT growth from a variety of factors, including gas pressure and growth time [110]. Sidewall defects can cause kinking of the nanotubes, which may contribute to the tortuous morphology of the tubes [107, 111]. The CVD film growth process typically produces CNTs with more defects and impurities than the pristine, short CNTs that give high k_{ind} values in individual CNT measurements [112]. Based on SEM and TEM analysis of these films, a majority of the tubes in the film are bundled [101]. Tube-tube coupling in the form of tube crossing or bundling may increase the number of phonon scattering sites along the CNT, causing lower k_{ind} [113]. Simulations by Berber *et al.* have shown that the interlayer interactions of stacked graphene sheets (graphite) lowered the thermal conductivity of a single sheet by nearly an order of magnitude and that the same should be expected of CNT bundles [114]. Measurements on bundled tubes have shown much lower k than single tubes, from ~2 to 683 W m^{-1} K^{-1} [115-117].

Figure 4-7d shows that R''_{base} ranges from 3 - 80 m^2 K^{-1} MW^{-1} for the thick samples. Only an upper bound could be determined for R''_{top} because the measurement loses sensitivity to R''_{top} as its value becomes small. R''_{top} is estimated to be 0.5 m^2 K^{-1} MW^{-1} or below for all samples because there is no expected thickness dependence of R''_{top} due to the base-side growth and the constant surface roughness with thickness. There is also no lower bound for R''_{base} for the thinnest three samples. High R''_{base} is possibly due to the poor thermal engagement between the CNTs and catalyst particles at the substrate, which may be related to the growth technique [98]. The ease in which CNT films delaminate from the substrate reflects this weak adhesion. There appears to be a trend of increasing R''_{base} with increasing thickness. This may be due to detachment of nanotubes from the base or increasing defect concentration with growth time, as mentioned earlier [24]. Thicker films seem to delaminate more easily during handling of the sample. Sample damage may cause variations between samples.

66

Though R''_{base} is large in some samples, in practical applications VACNT films would be soldered to the surrounding substrates [32, 77]. This would yield values of R''_{base} similar to R''_{top} for all film thicknesses, as R''_{top} represents CNTs bonded to metal. VACNT films that are solder bonded should have a total resistance close to the thermal resistance of the bulk film, defined as $R''_{film} = L_{film}/k_{film}$, because R''_{top} is an order of magnitude lower than R''_{film}. In this case, the total resistance of the film would be comparable to thermal greases, which have thermal resistances on the order of 10 m^2 K MW^{-1} [1]. R''_{film} is plotted against film thickness in Figure 4-8. R''_{film} is compared to values from past literature and to the thermal resistance of a typical layer of thermal grease, solder, and an "ideal" VACNT film. The data in this work (circled) is within the past range of data for multiwalled VACNT films. From observation of the past data, k_{film} tends to decrease with film thickness, with films <50 μm having nearly ideal performance and films >100 μm never performing better than solder. This may be indication that thicker films have lower engagement and higher defect density with growth time. It could also be an experimental effect, as it is difficult to measure thin films accurately and some of the high k_{film} values were calculated using assumptions about $C_{v,film}$ or k_{ind}.
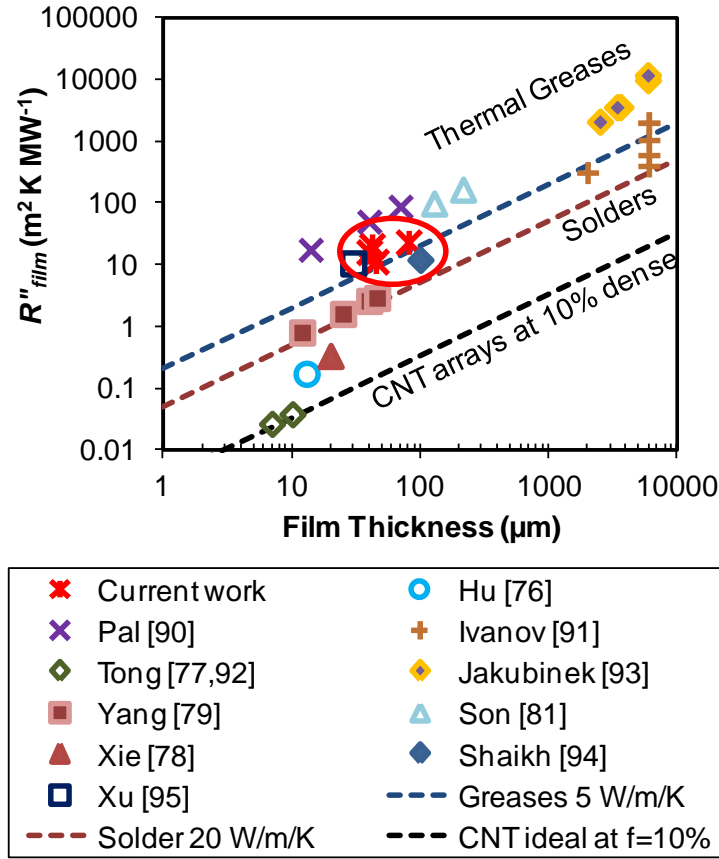
Figure 4-8: Thermal resistance of VACNT films, without boundary resistances. Because k_{film} is unknown for the films <40 μm, they are not plotted. The data are compared to grease at 5 W m^{-1} K^{-1}, solder at 20 W m^{-1} K^{-1}, and an "ideal" VACNT film with k_{ind} = 3000 W m^{-1} K^{-1} and f = 10% giving k_{film} = 300 W m^{-1} K^{-1}.

Figure 4-9 shows several representative image analysis results that may help elucidate trends in the thermal data. Figure 4-9a shows the CNT alignment in the film, represented by the aspect ratio which is the ratio of the average vertical tube-tube spacing to the average horizontal tube-tube spacing. The alignment peaks around 15 μm and decreases as growth time increases, similar to films observed in past work [24, 31]. Figure 4-9b shows f quantified by estimating the volume of tubes in a given volume of the film. f is calculated using an assumed bundle diameter of 5 nm – it does not represent an accurate comparison to the measured value of f. Using this

68

assumption, the density appears to be fairly constant through the film thickness and between films and does not exhibit previously observed density decay [24, 31]. Obtaining density information from SEM images is less accurate than the alignment due to the impact of the depth of field of the SEM, resulting in more scatter in f. In summary, observation of these SWCNT films shows that there are thickness-dependent effects which stem from the base side.
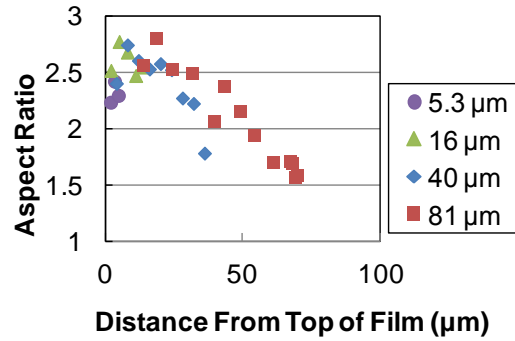
(a)
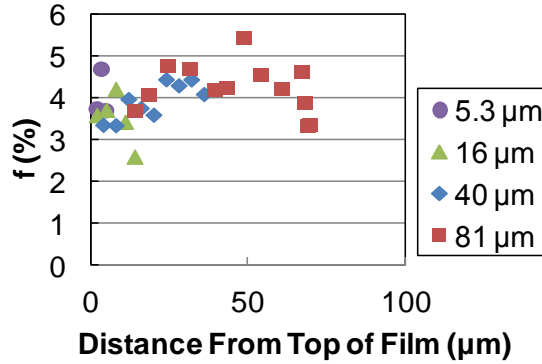
(b)

Figure 4-9: (a) Aspect ratio calculated from SEM images taken from the top to bottom of SWCNT films. The nanotubes grow from the base side, so the top of the film corresponds to initial growth. (b) Calculated f based on the same images as in (a). The calculation assumes a bundle diameter of 5 nm [101].

4.5   Solder Bonding of VACNT Films

The interface resistance of VACNT films has been shown to depend strongly on the quality of the bond between the film and surrounding substrates. This work includes initial development of a bonding method that involves soldering a VACNT film to new substrates using 25 μm-thick indium foil. Indium is one of the lowest melting temperature solders and was chosen for its availability and ease of use. In future studies a thinner foil or evaporated layer of indium can be used, in addition to other types of solder.

Figure 4-10 shows the stack of metals used for bonding a CNT film to a second substrate (*eg.* quartz). All surfaces to be soldered are coated using e-beam evaporation with a standard layering of metals consisting of Cr, Ni, and Au. The Cr acts as an adhesion layer while the Ni acts as a diffusion barrier for the Au. Au bonds well to In.
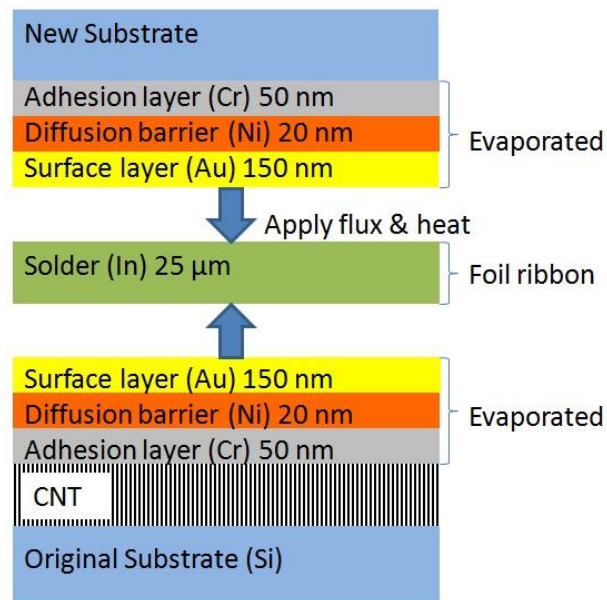
Figure 4-10: Schematic of layers of materials used in solder bonding, with thicknesses of each metal layer.

The bonding procedure requires all surfaces to be free of oxide, which can be accomplished by using flux or cleaning the indium foil immediately before soldering. Soldering is performed by placing the sample on a hotplate and heating it above the melting temperature of In under light pressure. After the sample cools the original Si substrate is pulled off the VACNT film, which remains bonded to the new substrate. The procedure can be repeated to bond the VACNT film to two new substrates, as shown in Figure 4-11. An alternate to indium foil which is appropriate for high temperature applications involves Nanofoil® (Indium Co.) and is described in Barako *et al.* [32].
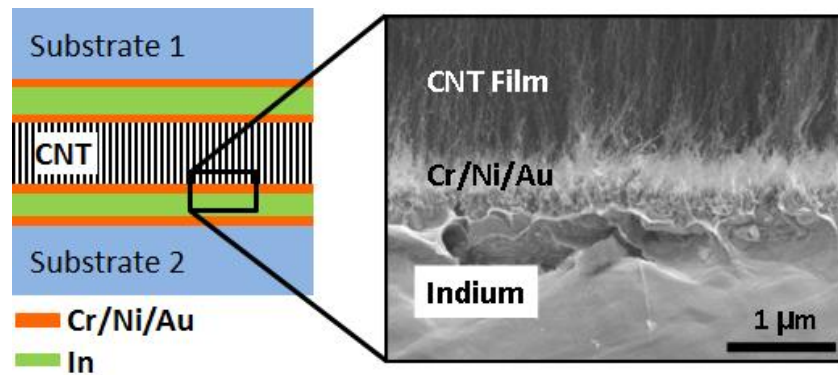
Figure 4-11: Schematic of a VACNT film bonded to two new substrates using In foil. An SEM shows the CNT-In bond.

Infrared microscopy is used to measure the boundary resistances of bonded films. The measurements are done in collaboration with Michael Barako and are described in Barako *et al.* [32]. Table 4-3 shows the dramatic differences between three types of interfaces. The first is the interface between a VACNT film simply pressed against another substrate, the second is the growth-side interface between an as-grown VACNT film and Si substrate, and the third is the interface between a VACNT film solder-bonded to another substrate. The first un-bonded case has the largest resistance because the nanotubes are not well contacted to the second substrate.

The growth interface resistance is an order of magnitude lower than the un-bonded interface because each nanotube is attached to the substrate. A soldered interface is an order of magnitude lower than the growth interface, reflecting the difference between the CNT-metal and CNT-substrate interfaces observed in Section 4.4 for the SWCNT films. Cola *et al.* showed that increasing the contact area at CNT-substrate interfaces reduces boundary resistance [118]. This may explain why a conformal metal coating results in a lower thermal resistance than at the CNT-substrate interface, where CNTs are perpendicular to the substrate.

Table 4-3: Interface resistances for an un-bonded interface ("Un-bonded"), the growth interface between a VACNT film and Si substrate ("Growth"), and an interface that has been bonded using In ("Indium Bonded").

Materials	Interface	R'' (m^2 K MW^{-1})
CNT-Quartz	Un-bonded	1150-1350
CNT-Si	Growth	235-270
CNT-Quartz	Indium Bonded	41-55

Figure 4-12 shows that the improvement in boundary resistance between bonded and un-bonded interfaces is over an order of magnitude even at higher pressure. The un-bonded interface does improve with pressure as more nanotubes are pressed against the second substrate. This indicates that thermal conduction between nanotubes and surrounding materials is poor unless the nanotube is fully joined to the surrounding substrates using a binder material such as solder. This also suggests that tube-tube contact resistance would improve if the tubes are coated with a binder material at the contact.
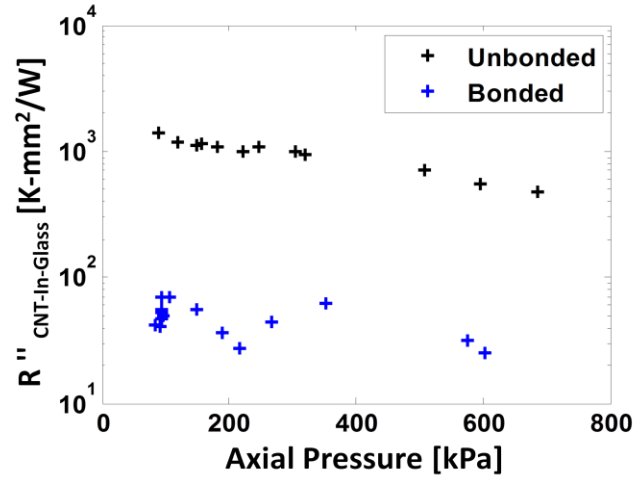
Figure 4-12: The interface resistance of an un-bonded and bonded interface under applied pressure [32].

Based on these results, VACNT films will likely have high thermal performance if both interfaces are bonded. Little literature exists on thermal measurement of VACNT films solder bonded on *both* sides, which is a subject of current research. Bonding studies were not performed on the SWCNT films described earlier because the supply of samples was limited. Also, the infrared microscopy method works best with films >100 μm due to the resolution of the camera.

4.6   Summary

This work presents the complete thermal properties of a set of vertically aligned SWCNT films ranging from 5.3 μm to 81 μm thick. The properties k_{film}, $C_{v,film}$, $R"_{top}$ and $R"_{base}$ are measured independently and the morphology of the films is studied using SEM and AFM. It is clear from the results that SWCNT films do not perform better than MWCNT films even though these samples had relatively high quality and alignment. Thermal measurements and image analysis show that the thermal properties may be related to the thickness of the film, because the film seems to be

increasingly disordered at the base as growth continues and R''_{base} appears to increase with film thickness. For many samples R''_{base} is an order of magnitude higher than R''_{top}. This finding is supported by bonding studies.

Quantifying the density and tortuosity of CNTs in a film can serve several purposes. Knowing the film structure can explain differences in measured properties between samples. This can also guide the growth process, if a certain structure and thermal property is desired. A model of the film's thermal properties based on structural information would enable prediction of the thermal performance of a CNT film.

Future improvements to the thermal performance of VACNT films include soldering bonding both surfaces of the film, increasing film density, and annealing of defects, which are all active areas of study in other work. At $f \sim 7\%$, there is potential to greatly increase the density of these films, either by modifying growth methods or mechanical densification. With these improvements VACNT films have the potential to consistently surpass the performance of solder TIMs.

Chapter 5   Conclusion

5.1   Summary

This thesis focuses on characterizing and understanding the properties of VACNT films relevant for TIM applications. Most of the challenges of this work are experimental in nature, such as the experimental setup and data analysis.

One contribution of this work is the comparison of the top and base side modulus of a set of multiwalled VACNT films to investigate modulus inhomogeneities within the VACNT film and between films. To accomplish this, a nanoindentation measurement technique is developed using an atomic force microscope and custom fabricated spherical indenter tips. The morphology of the film is examined using an image analysis procedure developed to extract nanotube alignment and density from SEM images. A modified cellular model links the modulus and image data. With the relationship between tube morphology and modulus known, the expected modulus of a given VACNT film can be calculated based on image data.

Several conclusions can be drawn from that study. The results show that the films have low modulus, as expected due to their high porosity and disorder, and are mechanically suitable as TIMs. The alignment of the nanotubes gradually varies with depth into the film. The alignment peaks about 50 μm below the film surface and then decreases as growth time progresses, reaching a minimum at the base. The modulus should follow a similar trend; this is supported by the low measured modulus at the base side. Calculations using the cellular model with geometric inputs from image data show that the out-of-plane modulus is up to an order of magnitude higher than the in-plane modulus. Film growth can be improved and adjusted using information about the CNT alignment. For example, if a high modulus is desired the growth can be

terminated during the period of highest alignment. This technique also represents a way to predict the mechanical behavior of a VACNT film using image data rather than performing complex mechanical measurements.

The first investigation into growing VACNT TIMs on thermoelectric materials is presented. While the implementation may be more complex than in traditional electronics, the rewards are greater. The thermal resistance of the layer is measured using nanosecond thermoreflectance. Thermal cycling showed that the film is stable after cycling up to 200 °C.

This work also measures four key thermal properties of a set of SWCNT films. The results indicate that k of SWCNT films is similar to that of MWCNT films. Tube-tube bundling may play a large role in the lower than expected k. The results also indicate that the CNT-substrate resistance is much higher than the CNT-metal interface resistance. Preliminary studies on solder bonding of VACNT films show that bonding significantly reduces boundary resistance.

As expected, the structure of VACNT films can influence its physical properties. This may be one reason that past data on VACNT films is inconsistent, as nanotube structure can vary widely. This also implies that the film can be designed or tuned to give the desired thermal and mechanical properties.

This work also illustrates the challenges of measuring VACNT films. These include many unknown properties, large errors in the data due to uncertainty in the experiment or sample structure, and difficulty in extracting specific properties such as local out-of-plane modulus or heat capacity. These challenges may be a significant contribution to the scatter in past data.

In summary, this work shows that these three aspects of thermal, mechanical, and morphological characterization of VACNT films should be done in conjunction to

fully understand the behavior of these complex films. Key film properties are identified that can be tuned to engineer an ideal VACNT TIM.

5.2   Discussion and Suggestions for Future Work

5.2.1   Future Work on Characterization and Modeling of VACNT Films

For TIM applications there are many more tests to perform. Reliability may be one of the major advantages of using CNT TIMs and the reliability of these films must be tested under actual and extreme operating conditions. This includes thermal cycling studies. CNTs may oxidize at higher temperatures, so for relevant applications the effects of oxidation would need to be studied. Preliminary thermal cycling performed in our group shows that the VACNT film thermal performance is stable up to 500 °C over hundreds of cycles.

Future work can also include development of a thermal model. There has been some modeling of the VACNT film k and interface resistances in the past [72, 118, 119], but the models are approximations and do not mimic the true alignment, tube-tube contact, and defect concentration in a VACNT film. Preliminary work has begun in utilizing a coarse-grained molecular model of the nanotube structure as the basis for a thermal model. The model was originally developed by Dr. Yoonjin Won and Professor Wei Cai at Stanford University to simulate the mechanical response of the film. The coarse-grained molecular model represents nanotubes as a series of nodes that interact through van der Waals interactions. These nanotubes are allowed to relax to their lowest energy state using an energy minimization routine. This bundling behavior results in a realistic film morphology that includes tube-tube bundling. The alignment and density of the nanotubes can be tuned to reflect those of an actual film and has given results for mechanical modulus similar to the cellular model. The molecular model can provide the tube length and tube-tube contact area information required for a thermal model. The defect density would have to be an assumed value or measured from an individual tube.

The methods in this work, including the experimental techniques and the combined measurement, image analysis, and modeling, can be applied to a variety of nanostructured materials. Other promising TIM materials include metal nanowire meshes and arrays that can be analyzed in a similar manner.

5.2.2 IMPROVEMENTS TO VACNT PROPERTIES

The major roadblocks towards implementation are on the thermal side. Though the mechanical behavior is complex, it surpasses the targeted compliance for TIM applications. Some thoughts on future improvements follow.

Two established techniques can improve the thermal conductivity of these films in future measurements. The first is densification of the film. Because the elastic modulus of these films is lower than required due to their high porosity, the film can be significantly compressed before becoming too stiff. The high density of tubes will increase k. Physical densification has been previously performed on VACNT films using techniques including biaxial compression [120] and water-assisted methods [121]. There has been some work on density-dependent thermal conductivity measurements of VACNT composites [122] but very little investigation into densified bare films. Though densification increases tube-tube contact, which may reduce k, the effect may not be large because many tubes are already bundled. In looking at past data of VACNT films plotted against f in Gao et al. [10], there is little evidence that density is detrimental to k. Densification studies will also provide a wealth of information about effects such as tube-tube coupling and tube alignment.

The second improvement is bonding the film to the surrounding substrates. The consistency and reproducibility of these processes need improvement, but the results in this work suggest that the interfaces between VACNT films and their surroundings are critical to the thermal performance of the film.

There is also a need to control the electrical conductivity of films for certain applications. Currently, VACNT films contain a random assortment of metallic and

78

semiconducting CNTs, properties determined by their chirality. Past work has shown that the chirality of CVD-grown CNT films depends on the structure of the catalyst [123] or the growth method [124]. Though many TIMs are not in an electrical pathway, certain TIM applications require electrical insulation, while others require electrical conductivity. The TEM application in Chapter 3 requires the TIM to be electrically conducting if it is to replace the solder bond.

The manufacturing and cost issues will be challenging for these TIMs. VACNT films do have the potential to be mass produced because there is no limit to the substrate size. The steps required to densify and bond a CNT film are relatively simple and can be performed on blanket films. CNT films remain promising and can be expected to compete with commercial TIMs after improvement of their thermal properties.

Bibliography

[1] R. Prasher, "Thermal Interface Materials: Historical Perspective, Status, and Future Directions," *Proceedings of the IEEE,* vol. 94, pp. 1571-1586, 2006.

[2] E. M. Petrie, *Handbook of Adhesives and Sealants*. New York: McGraw-Hill, 2000.

[3] F. Sarvar*, et al.*, "Thermal Interface Materials - A Review of the State of the Art," *Manufacturing Engineering,* pp. 1292-1302, 2006.

[4] C. Yu*, et al.*, "Thermal Conductance and Thermopower of an Individual Single-Wall Carbon Nanotube," *Nano Letters,* vol. 5, pp. 1842-1846, 2005.

[5] E. Pop*, et al.*, "Thermal Conductance of an Individual Single-Wall Carbon Nanotube above Room Temperature," *Nano Letters,* vol. 6, pp. 96-100, 2006.

[6] M. Fujii*, et al.*, "Measuring the Thermal Conductivity of a Single Carbon Nanotube," *Phys. Rev. Lett.,* vol. 95, p. 065502, 2005.

[7] P. Kim*, et al.*, "Thermal Transport Measurements of Individual Multiwalled Nanotubes," *Physical Review Letters,* vol. 87, p. 215502, 2001.

[8] O. Yaglioglu*, et al.*, "Conductive Carbon Nanotube Composite Microprobes," *Adv. Mater,* vol. 20, pp. 357-362, 2008.

[9] G. Zhang*, et al.*, "Ultra-high-yield growth of vertical single-walled carbon nanotubes: Hidden roles of hydrogen and oxygen," *Proceedings of the National Academy of Sciences of the United States of America,* vol. 102, pp. 16141-16145, November 8, 2005 2005.

[10] Y. Gao*, et al.*, "Nanostructured Interfaces for Thermoelectrics," *Journal of Electronic Materials,* vol. 39, pp. 1456-1462, 2010.

[11] E. Pop, *et al.*, "Thermal Conductance of an Individual Single-Wall Carbon Nanotube above Room Temperature," *Nano Letters,* vol. 6, pp. 96-100, 2005.

[12] T. Tong, *et al.*, "Dense Vertically Aligned Multiwalled Carbon Nanotube Arrays as Thermal Interface Materials," *IEEE T. Compon. Pack. T.,* vol. 30, pp. 92-100, 2007.

[13] S. D. Mesarovic, *et al.*, "Mechanical behavior of a carbon nanotube turf," *Scripta Materialia,* vol. 56, pp. 157-160, 2007.

[14] Q. Zhang, *et al.*, "Viscoelastic creep of vertically aligned carbon nanotubes," *Journal of Physics D: Applied Physics,* vol. 43, pp. 315401-7, 2010.

[15] C. M. McCarter, *et al.*, "Mechanical compliance of photolithographically defined vertically aligned carbon nanotube turf," *Journal of Materials Science,* vol. 41, pp. 7872-7878, 2006.

[16] A. A. Zbib, *et al.*, "The coordinated buckling of carbon nanotube turfs under uniform compression," *Nanotechnology,* vol. 19, pp. 175704-10, 2008.

[17] C. P. Deck, *et al.*, "Mechanical behavior of ultralong multiwalled carbon nanotube mats," *Journal of Applied Physics,* vol. 101, pp. 023512-9, 2007.

[18] A. Cao, *et al.*, "Super-Compressible Foamlike Carbon Nanotube Films," *Science,* vol. 310, pp. 1307-1310, November 25, 2005 2005.

[19] M. R. Maschmann, *et al.*, "Length dependent foam-like mechanical response of axially indented vertically oriented carbon nanotube arrays," *Carbon,* vol. 49, pp. 386-397, 2011.

[20] M. R. Maschmann, *et al.*, "In situ SEM Observation of Column-like and Foam-like CNT Array Nanoindentation," *ACS Applied Materials & Interfaces,* vol. 3, pp. 648-653, 2011.

[21] B. Yurdumakan, *et al.*, "Synthetic gecko foot-hairs from multiwalled carbon nanotubes," *Chemical Communications,* pp. 3799-3801, 2005.

[22] Y. Won, *et al.*, "Mechanical characterization of aligned multi-walled carbon nanotube films using microfabricated resonators," *Carbon,* vol. 50, pp. 347-355, 2012.

[23]   L. Zhang, *et al.*, "Influence of a Top Crust of Entangled Nanotubes on the Structure of Vertically Aligned Forests of Single-Walled Carbon Nanotubes," *Chemistry of Materials,* vol. 18, pp. 5624-5629, 2006.

[24]   M. Bedewy, *et al.*, "Collective Mechanism for the Evolution and Self-Termination of Vertically Aligned Carbon Nanotube Growth," *The Journal of Physical Chemistry C,* vol. 113, pp. 20576-20582, 2009.

[25]   B. N. Wang, *et al.*, "Quantitative Characterization of the Morphology of Multiwall Carbon Nanotube Films by Small-Angle X-ray Scattering," *The Journal of Physical Chemistry C,* vol. 111, pp. 5859-5865, 2007.

[26]   H. Malik, *et al.*, "Quantitative characterization of carbon nanotube turf topology by SEM analysis," *Journal of Materials Science,* vol. 46, pp. 3119-3126, 2011.

[27]   M. A. Al-Khedher, *et al.*, "Quality classification via Raman identification and SEM analysis of carbon nanotube bundles using artificial neural networks," *Nanotechnology,* vol. 18, pp. 355703-355713, 2007.

[28]   S. B. Hutchens, *et al.*, "Analysis of uniaxial compression of vertically aligned carbon nanotubes," *Journal of the Mechanics and Physics of Solids,* vol. 59, pp. 2227-2237, 2011.

[29]   S. B. Hutchens, *et al.*, "In situ Mechanical Testing Reveals Periodic Buckle Nucleation and Propagation in Carbon Nanotube Bundles," *Advanced Functional Materials,* vol. 20, pp. 2338-2346, 2010.

[30]   A. Qiu, *et al.*, "Spatial Variations in the Mechanical Properties and Electrical Properties of Carbon Nanotube Turfs.," *MRS Proceedings,* vol. 1258, pp. 1258-R10-29, 2010.

[31]   Y. Gao, *et al.*, "Impact of nanotube density and alignment on the elastic modulus near the top and base surfaces of aligned multi-walled carbon nanotube films," *Carbon,* vol. 50, pp. 3789-3798, 2012.

[32]   M. T. Barako, *et al.*, "Solder Bonding for Carbon Nanotube-based Thermal Interface Materials," *Proc. ITherm 2012,* 2012.

[33]   J. E. Sader, *et al.*, "Calibration of rectangular atomic force microscope cantilevers," vol. 70, pp. 3967-3969, 1999.

[34]   T. Kodama, *et al.*, "Atomic force microscope equipped with confocal laser scanning microscope for the spectroscopic measurement of the contact area in liquid," *Chemical Physics Letters,* vol. 385, pp. 507-511, 2004.

[35]   M. L. Oyen, *Handbook of Nanoindentation: With Biological Applications*: Pan Stanford Publishing, 2010.

[36]   H.-J. Butt, *et al.*, "Force measurements with the atomic force microscope: Technique, interpretation and applications," *Surface Science Reports,* vol. 59, pp. 1-152, 2005.

[37]   M. Jaschke and H.-J. Butt, "Height calibration of optical lever atomic force microscopes by simple laser interferometry," *Review of Scientific Instruments,* vol. 66, pp. 1258-1259, 1995.

[38]   L.-O. Heim, *et al.*, "Tilt of Atomic Force Microscope Cantilevers: Effect on Spring Constant and Adhesion Measurements," *Langmuir,* vol. 20, pp. 2760-2764, 2004.

[39]   W. C. Oliver and G. M. Pharr, "An improved technique for determining hardness and elastic modulus using load and displacement sensing indentation experiments," *J. Mater. Res.,* vol. 7, p. 1564, 1992.

[40]   D. M. Ebenstein and K. J. Wahl, "A comparison of JKR-based methods to analyze quasi-static and dynamic indentation force curves," *Journal of Colloid and Interface Science,* vol. 298, pp. 652-662, 2006.

[41]   Y. Zhao, *et al.*, "Interfacial energy and strength of multiwalled-carbon-nanotube-based dry adhesive," *Journal of Vacuum Science & Technology B: Microelectronics and Nanometer Structures,* vol. 24, pp. 331-335, 2006.

[42]   K. L. Johnson, *et al.*, "Surface Energy and the Contact of Elastic Solids," *Proceedings of the Royal Society of London. A. Mathematical and Physical Sciences,* vol. 324, pp. 301-313, September 8, 1971 1971.

[43]   D. Tabor, "Surface forces and surface interactions," *Journal of Colloid and Interface Science,* vol. 58, pp. 2-13, 1977.

[44]   W.-G. Jiang, *et al.*, "Effect of surface roughness on nanoindentation test of thin films," *Engineering Fracture Mechanics,* vol. 75, pp. 4965-4972, 2008.

[45]   C. Walter, *et al.*, "Finite element simulation of the effect of surface roughness on nanoindentation of thin films with spherical indenters," *Surface and Coatings Technology,* vol. 202, pp. 1103-1107, 2007.

[46]   Suhr J, *et al.*, "Fatigue resistance of aligned carbon nanotube arrays under cyclic compression," *Nat Nano,* vol. 2, pp. 417-421, 2007.

[47]   J.-Y. Kim, *et al.*, "Influence of surface-roughness on indentation size effect," *Acta Materialia,* vol. 55, pp. 3555-3562, 2007.

[48]   J. Menčík, *et al.*, "Determination of elastic modulus of thin layers using nanoindentation.," *Journal of Materials Research,* vol. 12, pp. 2475-2484, 1997.

[49]   C. Pailler-Mattei, *et al.*, "In vivo measurements of the elastic mechanical properties of human skin by indentation tests," *Medical Engineering & Physics,* vol. 30, pp. 599-606, 2008.

[50]   A. Perriot and E. Barthel, "Elastic contact to a coated half-space: Effective elastic modulus and real penetration.," *Journal of Materials Research,* vol. 19, pp. 600-608 2004.

[51]   J. J. Vlassak and W. D. Nix, "Indentation modulus of elastically anisotropic half spaces," *Philosophical Magazine A,* vol. 67, pp. 1045-1056, 1993/05/01 1993.

[52]   J. G. Swadener and G. M. Pharr, "Indentation of elastically anisotropic half-spaces by cones and parabolae of revolution," *Philosophical Magazine A,* vol. 81, pp. 447-466, 2001.

[53]   W. Wang and K. Lu, "Nanoindentation study on elastic and plastic anisotropies of Cu single crystals," *Philosophical Magazine,* vol. 86, pp. 5309-5320, 2006/11/21 2006.

[54]   F. Schneider, *et al.*, "Mechanical properties of silicones for MEMS," *Journal of Micromechanics and Microengineering,* vol. 18, pp. 065008-16, 2008.

[55] S.-J. Park, *et al.*, "Analysis of nematode mechanics by piezoresistive displacement clamp," *Proceedings of the National Academy of Sciences,* vol. 104, pp. 17376-17381, October 30, 2007 2007.

[56] L. J. Gibson and M. F. Ashby, *Cellular Solids: Structure and Properties*, 2 ed. Cambridge, UK: Cambridge University Press, 1997.

[57] B. G. Demczyk, *et al.*, "Direct mechanical measurement of the tensile strength and elastic modulus of multiwalled carbon nanotubes," *Materials Science and Engineering: A,* vol. 334, pp. 173-178, 2002.

[58] E. E. Underwood, *Quantitative Stereology*. Reading, MA: Addison-Wesley Publishing Co, 1970.

[59] V. Ravi, *et al.*, "Thermal Expansion Studies of Selected High-Temperature Thermoelectric Materials," *Journal of Electronic Materials,* vol. 38, pp. 1433-1442, 2009.

[60] M. Srinivasan and S. M. Praslad, "Advanced Thermoelectric Energy Recovery System in Light Duty and Heavy Duty Vehicles: Analysis on Technical and Marketing Challenges," in *Int. Conf. Power Electron. Drives Sys.*, 2005, pp. 977-982.

[61] X. C. Xuan, *et al.*, "A general model for studying effects of interface layers on thermoelectric devices performance," *International Journal of Heat and Mass Transfer,* vol. 45, pp. 5159-5170, 2002.

[62] G. Min and D. M. Rowe, "Cooling performance of integrated thermoelectric microcooler," *Solid-State Electronics,* vol. 43, pp. 923-929, 1999.

[63] T. J. Hendricks and J. A. Lustbader, "Advanced Thermoelectric Power System Investigations for Light-Duty and Heavy-Duty Vehicle Applications: Part II," in *Proceedings of the 21st International Conference on Thermoelectrics*, Long Beach, CA, 2002, pp. pp. 387–394.

[64] I. Chowdhury, *et al.*, "On-chip cooling by superlattice-based thin-film thermoelectrics," *Nature Nanotechnology,* vol. 4, pp. 235-238, 2009.

[65] A. Pettes, *et al.*, "Optimized Thermoelectric Refrigeration in the Presence of Thermal Boundary Resistance," *Proc. IPACK2007,* vol. 2, pp. 221-228, 2007.

[66]   S. LeBlanc and Y. Gao, "Thermoelectric Heat Recovery from a Tankless Water Heating System," in *Proc. IMECE*, Boston, MA, 2008.

[67]   T. Clin*, et al.*, "Numerical Simulation of the Thermomechanical Behavior of Extruded Bismuth Telluride Alloy Module," *Journal of Electronic Materials,* vol. 38, pp. 994-1001, 2009.

[68]   Y. Hori*, et al.*, "Analysis on thermo-mechanical stress of thermoelectric module," *Eighteenth International Conference on Thermoelectrics,* pp. 328-331, 1999.

[69]   J. Vázquez*, et al.*, "State of the Art of Thermoelectric Generators Based on Heat Recovered from the Exhaust Gases of Automobiles," in *Proc. 7th European Workshop Thermoelect.*, Pamplona, Spain, 2002, p. p. 17.

[70]   C. M. Bhandari and D. M. Rowe, "Silicon - germanium alloys as high-temperature thermoelectric materials," *Contemporary Physics,* vol. 21, pp. 219 - 242, 1980.

[71]   A. Shakouri, "Nanoscale Thermal Transport and Microrefrigerators on a Chip," *Proceedings of the IEEE,* vol. 94, pp. 1613-1638, 2006.

[72]   M. A. Panzer*, et al.*, "Thermal Properties of Metal-Coated Vertically Aligned Single-Wall Nanotube Arrays," *Journal of Heat Transfer,* vol. 130, pp. 052401-9, 2008.

[73]   B. M. Clemens*, et al.*, "Time-resolved thermal transport in compositionally modulated metal films," *Phys. Rev. B,* vol. 37, p. 1085, 1988.

[74]   D. G. Cahill, "Analysis of Heat flow in Layered Structures for Time-domain Thermoreflectance," *Review of Scientific Instruments,* vol. 75, pp. 5119-5122, 2004.

[75]   B. A. Cola*, et al.*, "Photoacoustic Characterization of Carbon Nanotube Array Thermal Interfaces," *J. of Appl. Phys.,* vol. 101, pp. 054313-9, 2007.

[76]   X. J. Hu*, et al.*, "3-Omega Measurements of Vertically Oriented Carbon Nanotubes on Silicon," *Journal of Heat Transfer,* vol. 128, pp. 1109-1113, 2006.

[77]   T. Tong, *et al.*, "Dense Vertically Aligned Multiwalled Carbon Nanotube Arrays as Thermal Interface Materials," *IEEE Transactions on Components and Packaging Technologies,* vol. 30, pp. 92-100, 2007.

[78]   H. Xie, *et al.*, "Thermal diffusivity and conductivity of multiwalled carbon nanotube arrays," *Physics Letters A,* vol. 369, pp. 120-123, 2007.

[79]   D. J. Yang, *et al.*, "Thermal conductivity of multiwalled carbon nanotubes," *Physical Review B,* vol. 66, p. 165440, 2002.

[80]   X. Wang, *et al.*, "Noncontact thermal characterization of multiwall carbon nanotubes," *Journal of Applied Physics,* vol. 97, pp. 064302-5, 2005.

[81]   Y. Son, *et al.*, "Thermal resistance of the native interface between vertically aligned multiwalled carbon nanotube arrays and their SiO[sub 2]/Si substrate," *Journal of Applied Physics,* vol. 103, pp. 024911-7, 2008.

[82]   F. Sarvar, *et al.*, "Thermal Interface Materials - A Review of the State of the Art," in *Electronics Systemintegration Technology Conference, 2006.*, 2006, pp. 1292-1302.

[83]   Y. Yun, *et al.*, "Growth Mechanism of Long Aligned Multiwall Carbon Nanotube Arrays by Water-Assisted Chemical Vapor Deposition," *The Journal of Physical Chemistry B,* vol. 110, pp. 23920-23925, 2006.

[84]   M. P. Prahalad and et al., "A generic process of growing aligned carbon nanotube arrays on metals and metal alloys," *Nanotechnology,* vol. 18, p. 185605, 2007.

[85]   S. Maruyama, "A Molecular Dynamics Simulation of Heat Conduction of a Finite Length Single-Walled Carbon Nanotube," *Microscale Thermophysical Engineering,* vol. 7, pp. 41 - 50, 2003.

[86]   J. Shiomi and S. Maruyama, "Molecular Dynamics of Diffusive-Ballistic Heat Conduction in Single-Walled Carbon Nanotubes," *Jpn. J. Appl. Phys.,* vol. 47, pp. 2005-2009, 2008.

[87]   M. T. Pettes and L. Shi, "Thermal and Structural Characterizations of Individual Single-, Double-, and Multi-Walled Carbon Nanotubes," *Advanced Functional Materials,* vol. 19, pp. 3918-3925, 2009.

[88]   K. Hata*, et al.*, "Water-Assisted Highly Efficient Synthesis of Impurity-Free Single-Walled Carbon Nanotubes," *Science,* vol. 306, pp. 1362-1364, November 19, 2004 2004.

[89]   Y. Murakami*, et al.*, "Growth of vertically aligned single-walled carbon nanotube films on quartz substrates and their optical anisotropy," *Chemical Physics Letters,* vol. 385, pp. 298-303, 2004.

[90]   S. K. Pal*, et al.*, "Thermal and electrical transport along MWCNT arrays grown on Inconel substrates," *Journal of Materials Research,* vol. 23, p. 2099, 2008.

[91]   I. Ivanov*, et al.*, "Fast and highly anisotropic thermal transport through vertically aligned carbon nanotube arrays," *Applied Physics Letters,* vol. 89, pp. 223110-3, 2006.

[92]   T. Tong*, et al.*, "Indium Assisted Multiwalled Carbon Nanotube Array Thermal Interface Materials," in *ITHERM '06*, 2006, pp. 1406-1411.

[93]   M. B. Jakubinek*, et al.*, "Thermal and electrical conductivity of tall, vertically aligned carbon nanotube arrays," *Carbon,* vol. 48, pp. 3947-3952, 2010.

[94]   S. Shaikh*, et al.*, "Thermal conductivity of an aligned carbon nanotube array," *Carbon,* vol. 45, pp. 2608-2613, 2007.

[95]   Y. Xu*, et al.*, "Thermal properties of carbon nanotube array used for integrated circuit cooling," *Journal of Applied Physics,* vol. 100, pp. 074302-5, 2006.

[96]   M. A. Panzer*, et al.*, "Thermal Properties of Metal-Coated Vertically Aligned Single-Wall Nanotube Arrays," *Journal of Heat Transfer,* vol. 130, p. 052401, 2008.

[97]   R. Xiang*, et al.*, "Growth Deceleration of Vertically Aligned Carbon Nanotube Arrays: Catalyst Deactivation or Feedstock Diffusion Controlled?," *The Journal of Physical Chemistry C,* vol. 112, pp. 4892-4896, 2008.

[98]   M. A. Panzer*, et al.*, "Temperature-Dependent Phonon Conduction and Nanotube Engagement in Metalized Single Wall Carbon Nanotube Films," *Nano Letters,* vol. 10, pp. 2395-2400, 2010.

[99]   E. Einarsson*, et al.*, "Growth Mechanism and Internal Structure of Vertically Aligned Single-Walled Carbon Nanotubes," *Journal of Nanoscience and Nanotechnology,* vol. 8, pp. 6093-6098, 2008.

[100]   S. Maruyama*, et al.*, "Low-temperature synthesis of high-purity single-walled carbon nanotubes from alcohol," *Chemical Physics Letters,* vol. 360, pp. 229-234, 2002.

[101]   E. Einarsson*, et al.*, "Revealing the Small-Bundle Internal Structure of Vertically Aligned Single-Walled Carbon Nanotube Films," *The Journal of Physical Chemistry C,* vol. 111, pp. 17861-17864, 2007.

[102]   O. W. Kading*, et al.*, "Thermal conduction in metallized silicon-dioxide layers on silicon," *Applied Physics Letters,* vol. 65, pp. 1629-1631, 1994.

[103]   A. J. Schmidt*, et al.*, "A frequency-domain thermoreflectance method for the characterization of thermal properties," *Review of Scientific Instruments,* vol. 80, p. 094901, 2009.

[104]   J. A. Malen*, et al.*, "Optical Measurement of Thermal Conductivity Using Fiber Aligned Frequency Domain Thermoreflectance," *Journal of Heat Transfer,* vol. 133, p. 081601, 2011.

[105]   A. J. Schmidt*, et al.*, "A frequency-domain thermoreflectance method for the characterization of thermal properties," *Review of Scientific Instruments,* vol. 80, pp. 094901-6, 2009.

[106]   T. Borca-Tasciuc*, et al.*, "Anisotropic thermal diffusivity of aligned multiwall carbon nanotube arrays," *Journal of Applied Physics,* vol. 98, pp. 054309-6, 2005.

[107]   J. Che*, et al.*, "Thermal conductivity of carbon nanotubes," *Nanotechnology,* vol. 11, p. 65, 2000.

[108]   G. Zhang and B. Li, "Thermal conductivity of nanotubes revisited: Effects of chirality, isotope impurity, tube length, and temperature," *The Journal of Chemical Physics,* vol. 123, pp. 114714-4, 2005.

[109] S. Maruyama, *et al.*, "Anisotropic Heat Transfer of Single-Walled Carbon Nanotubes," *Journal of Thermal Science and Technology,* vol. 1, pp. 138-148, 2006.

[110] H. Cui, *et al.*, "Growth behavior of carbon nanotubes on multilayered metal catalyst film in chemical vapor deposition," *Chemical Physics Letters,* vol. 374, pp. 222-228, 2003.

[111] E. T. Thostenson, *et al.*, "Advances in the science and technology of carbon nanotubes and their composites: a review," *Composites Science and Technology,* vol. 61, pp. 1899-1912, 2001.

[112] M. Sveningsson, *et al.*, "Electron field emission from multi-walled carbon nanotubes," *Carbon,* vol. 42, pp. 1165-1168, 2004.

[113] A. E. Aliev, *et al.*, "Thermal conductivity of multi-walled carbon nanotube sheets: radiation losses and quenching of phonon modes," *Nanotechnology,* vol. 21, p. 035709, 2010.

[114] S. Berber, *et al.*, "Unusually High Thermal Conductivity of Carbon Nanotubes," *Physical Review Letters,* vol. 84, p. 4613, 2000.

[115] L. Shi, *et al.*, "Measuring Thermal and Thermoelectric Properties of One-Dimensional Nanostructures Using a Microfabricated Device," *Journal of Heat Transfer,* vol. 125, pp. 881-888, 2003.

[116] I. K. Hsu, *et al.*, "Optical Absorption and Thermal Transport of Individual Suspended Carbon Nanotube Bundles," *Nano Letters,* vol. 9, pp. 590-594, 2009/02/11 2009.

[117] J. Hone, *et al.*, "Electrical and thermal transport properties of magnetically aligned single wall carbon nanotube films," *Applied Physics Letters,* vol. 77, pp. 666-668, 2000.

[118] B. A. Cola, *et al.*, "Contact mechanics and thermal conductance of carbon nanotube array interfaces," *International Journal of Heat and Mass Transfer,* vol. 52, pp. 3490-3503, 2009.

[119]   A. N. Volkov and L. V. Zhigilei, "Scaling Laws and Mesoscopic Modeling of Thermal Conductivity in Carbon Nanotube Materials," *Physical Review Letters,* vol. 104, p. 215902, 2010.

[120]   B. L. Wardle*, et al.*, "Fabrication and Characterization of Ultrahigh-Volume-Fraction Aligned Carbon Nanotube–Polymer Composites," *Advanced Materials,* vol. 20, pp. 2707-2714, 2008.

[121]   D. N. Futaba*, et al.*, "Shape-engineerable and highly densely packed single-walled carbon nanotubes and their application as super-capacitor electrodes," *Nat Mater,* vol. 5, pp. 987-994, 2006.

[122]   A. M. Marconnet*, et al.*, "Thermal Conduction in Aligned Carbon Nanotube–Polymer Nanocomposites with High Packing Density," *ACS Nano,* vol. 5, pp. 4818-4825, 2011/06/28 2011.

[123]   H. Zhu*, et al.*, "A strategy to control the chirality of single-walled carbon nanotubes," *Journal of Crystal Growth,* vol. 310, pp. 5473-5476, 2008.

[124]   Y. Li*, et al.*, "Preferential Growth of Semiconducting Single-Walled Carbon Nanotubes by a Plasma Enhanced CVD Method," *Nano Letters,* vol. 4, pp. 317-321, 2004/02/01 2004.